J. Fluid Mech. (2023), *vol*. 967, A7, doi:10.1017/jfm.2023.450

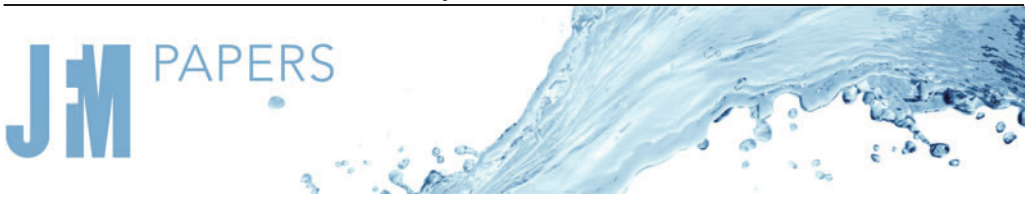

Influence of heterogeneity or shape on the locomotion of a caged squirmer

U. Aymen[1], D. Palaniappan[2], E. Demir[3],† and H. Nganguia[1],†

[1]Department of Mathematics, Towson University, Towson, MD 21252, USA

[2]Department of Mathematics and Statistics, Texas A&M University–Corpus Christi, Corpus Christi, TX 78412, USA

[3]Department of Mechanical Engineering and Mechanics, Lehigh University, Bethlehem, PA 18105, USA

(Received 10 February 2023; revised 29 May 2023; accepted 29 May 2023)

The development of novel drug delivery systems, which are revolutionizing modern medicine, is benefiting from studies on microorganisms' swimming. In this paper we consider a model microorganism (a squirmer) enclosed in a viscous droplet to investigate the effects of medium heterogeneity or geometry on the propulsion speed of the caged squirmer. We first consider the squirmer and droplet to be spherical (no shape effects) and derive exact solutions for the equations governing the problem. For a squirmer with purely tangential surface velocity, the squirmer is always able to move inside the droplet (even when the latter ceases to move as a result of large fluid resistance of the heterogeneous medium). Adding radial modes to the surface velocity, we establish a new condition for the existence of a co-swimming speed (where squirmer and droplet move at the same speed). Next, to probe the effects of geometry on propulsion, we consider the squirmer and droplet to be in Newtonian fluids. For a squirmer with purely tangential surface velocity, numerical simulations reveal a strong dependence of the squirmer's speed on shapes, the size of the droplet and the viscosity contrast. We found that the squirmer speed is largest when the droplet size and squirmer's eccentricity are small, and the viscosity contrast is large. For co-swimming, our results reveal a complex, non-trivial interplay between the various factors that combine to yield the squirmer's propulsion speed. Taken together, our study provides several considerations for the efficient design of future drug delivery systems.

Key words: swimming/flying, multiphase flow

† Email addresses for correspondence: demir@lehigh.edu, hnganguia@towson.edu

1. Introduction

The past few decades have seen tremendous progress in modern medicine, especially in the ways drugs and treatments are administered. Targeted drug delivery, a class of methods to deliver medication to specific organs or tissues, is showing great promise for patient care. One form of targeted drug delivery consists of inserting the drug in a micro- or nano-particle, called a carrier (Samanta, Hosseini-Nassab & Zare 2016; Kolosnjaj-Tabi *et al.* 2019; Wei *et al.* 2020; Chang *et al.* 2021; Kemp & Kwon 2021; Zhang, Liu & Zhang 2021; Fabozzi *et al.* 2023) that is then absorbed by the patient orally or via an injection. By using these carriers, the drug is kept from interacting with and affecting any healthy cells, tissues and organs as it safely makes its way through the bloodstream, thus minimizing negative side effects to the whole physiological system. Two features must be considered for effective and efficient drug delivery using carriers: design and control. Design must account for various factors, including shape (Liu *et al.* 2012; Nejati *et al.* 2020). Experimental and numerical studies have shown that under flow conditions and in the presence of red blood cells, non-spherical shapes (including ellipsoids) display a better margination rate (localization towards the blood vessel walls) compared with spherical particles. This enhanced rate is particularly important for the carrier's ability to adhere and ultimately cross biological barriers (Cooley *et al.* 2018; Mitchell *et al.* 2021). Control on the other end relies in part on the use of micro-robots that mimic the propulsion of biological microorganisms (Wu *et al.* 2020). The propulsion of microorganisms in unbounded fluids and media has attracted a tremendous amount of interest since the pioneering works of Taylor (1951) and Lighthill (1952). Studies have since extended these seminal works to investigate the propulsion of microorganisms in unbounded non-Newtonian and heterogeneous media (Yu, Lauga & Hosoi 2006; Lauga 2007; Leshansky 2009; Zhu *et al.* 2011; Pak *et al.* 2012; Datt *et al.* 2015; Chisholm *et al.* 2016; Lauga 2016; Gómez *et al.* 2017; Nganguia & Pak 2018). However, the use of carriers to enhance targeted drug delivery (Lee & Yeo 2015; Wu *et al.* 2020) or the development of nanotechnologies to manipulate cells in confined spaces (Raveshi *et al.* 2021) have led to increasing interest in the motion of microorganisms enclosed in various interfaces (Mirbagheri & Fu 2016; Reigh & Lauga 2017; Reigh *et al.* 2017; Daddi-Moussa-Ider, Lowen & Gekle 2018; Hoell *et al.* 2019; Nganguia *et al.* 2020*b*). One way of investigating the effects of these interfaces on propulsion is by considering the locomotion inside a closed domain. To this end, systems consisting of motile organisms enclosed in droplets have been designed (Clausal-Tormos *et al.* 2008; Wen *et al.* 2015; Ding *et al.* 2016; Raveshi *et al.* 2021). Recent theoretical studies of such systems assumed physical interfaces with various properties (Reigh *et al.* 2017; Shaik, Vasani & Ardekani 2018; Sprenger *et al.* 2020; Kree, Ruckert & Zippelius 2021; Kree & Zippelius 2021; Marshall & Brady 2021). In Reigh *et al.* (2017) the authors considered a squirmer inside a clean droplet and obtained analytical solutions for the squirmer and droplet speeds in a concentric configuration (the squirmer and droplet share the same centre). With this configuration, they showed that the squirmer always moves faster than the droplet. However, a co-swimming state (equal speeds between squirmer and droplet) can be achieved by considering radial modes in the surface velocity of the squirmer. The authors further analysed the stability of the co-swimming state numerically by considering various eccentric configurations. A surfactant-covered droplet has also been considered in place of a clean droplet (Shaik *et al.* 2018). As in Reigh *et al.* (2017), the authors of the study concluded that the squirmer propels faster than the droplet, yielding an unstable concentric configuration. The authors went on to show that various eccentric configurations, in which the squirmer and droplet no longer share the same centre of mass, led to a stable

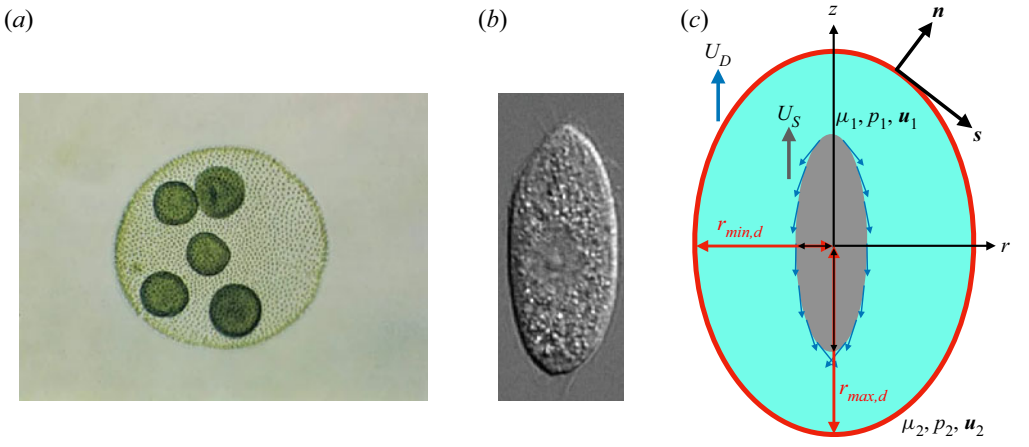

Figure 1. The squirmer represents ciliated microorganisms that can be approximated by (*a*) spherical shapes such as *Volvox* (adapted from https://www.britannica.com/science/Volvox/images-videos) or (*b*) spheroidal shapes such as *Tetrahymena thermophila* (reproduced from van Gogh *et al.* (2022), which is distributed under the terms of the Creative Common CC BY license). (*c*) Geometric set-up and schematic of a squirmer in a Newtonian fluid pocket with viscosity μ_1 enclosed in a droplet in a heterogeneous medium with viscosity μ_2. Both the squirmer and droplet are spheroids with semi-major and semi-minor axes $r_{maj,k}$ and $r_{min,k}$, respectively, where $k = s$ denotes the squirmer and $k = d$ denotes the droplet. (For spherically shaped squirmers and/or droplets, $r_{maj,k} = r_{min,k}$.) Here $\boldsymbol{n}$ and $\boldsymbol{s}$ denote the unit normal and tangent vectors to the spheroidal surfaces, respectively. The squirmer and droplet propel with speeds U_S and U_D, respectively.

co-swimming state. These recent findings have provided important insights on locomotion inside a droplet. The studies showed that the system can be tuned to achieve specific stable, co-swimming configurations. However, the results are limited to spherical squirmers enclosed in droplets in homogeneous Newtonian fluids. In reality, microorganisms often encounter heterogeneous environments with networks of obstacles embedded into viscous fluid media. For instance, spermatozoa navigate through cervical mucus with a filamentous network (Rutllant, Lopez-Bejar & Lopez-Gatius 2005); some spirochetes swim through highly complex and heterogeneous media and cross the blood-brain barrier to infect the brain (Radolf & Lukehart 2006; Wolgemuth 2015); bacteria *Helicobacter pylori* can invade the epithelial cells by moving through the gastric mucus gel that protects the stomach (Celli *et al.* 2009; Mirbagheri & Fu 2016). The presence of a sparse network of stationary obstacles embedded in an incompressible Newtonian fluid can be modelled using the Brinkman equations (Brinkman 1949) that include the additional hydrodynamic resistance due to the network of stationary obstacles. The Brinkman equations have been employed to address the effects of a viscous heterogeneous environment on locomotion performance (Leshansky 2009; Jung 2010; Leiderman & Olson 2016). In addition to the viscous heterogeneous environment, it was found that the swimming speed can be enhanced for specific combinations of permeability and geometric parameters of the swimmer (Leiderman & Olson 2016).

The squirmer model by Lighthill (1952) and Blake (1971) is adequate for spherically shaped ciliated organisms like *Volvox* (figure 1*a*). However, with a mean length-to-width aspect ratio of approximately 2, non-spherical ciliates are in fact more common (Lisicki *et al.* 2019; Rodrigues, Lisicki & Lauga 2021). Thus, a description of the squirmer that accounts for spheroidal geometry is needed to describe ciliated propulsion. Keller & Wu (1977) generalized the squirmer model to a prolate spheroidal body of arbitrary eccentricity that better represent organisms such as *Paramecium* and *Tetrahymena* (see

figure 1*b*). The theoretical prediction of their spheroidal model found good agreement with experimental data of freely swimming and inert sedimenting *Paramecium caudatum*. Further generalization of the spheroidal model in Keller & Wu (1977) has been proposed to include higher modes of swimming to represent other types of swimmers (Ishimoto & Gaffney 2014; Theers *et al.* 2016; Pohnl, Popescu & Uspal 2020), or to account for the effect of shape on squirming in non-Newtonian fluids (van Gogh *et al.* 2022). In addition to representing ciliates with spheroidal bodies, the spheroidal model serves as a first approximation to other non-spherical swimmers (e.g. *Escherichia coli*) to assess how geometrical shape affects swimming performance. We examine the dependence of caged microorganisms' propulsion on (1) fluid heterogeneity (to model *in vivo* biological environments), and (2) squirmer and droplet shapes (for the control and design of micro-robots and drug carriers). The paper is organized as follows. First, we describe the setting and formulate the problem in § 2, which includes a discussion of the analytical (§ 2.2) and numerical (§ 2.3) methods employed in our study. We then derive the propulsion speeds of the spherical squirmer and droplets in § 3, validate our results against previous studies in § 3.1, and proceed to investigate the effects of the fluid resistance on the squirmer-droplet system (§ 3.2) and on its co-swimming state (§ 3.3). The second half of our study, § 4, investigates the effects of non-spherical squirmer and/or droplet shapes on propulsion in a homogeneous, Newtonian fluid. We analyse shape effects on the squirmer's individual (§ 4.1) and co-swimming (§ 4.2) speeds. The consideration of shapes reveal many interesting results that we further analyse by looking at the pressure and velocity profiles from the various configurations (§ 4.3). Finally, we summarize our findings in § 5 and discuss implications for current and future designs of drug delivery systems.

2. Formulation

We consider the propulsion of a spheroidal squirmer in an homogeneous Newtonian pocket encapsulated inside a spheroidal droplet in an heterogeneous medium, as illustrated in figure 1(*c*). The spheroidal squirmers and droplets have semi-major and semi-minor axes $r_{maj,k}$ and $r_{min,k}$, respectively, where $k = s$ denotes the squirmer and $k = d$ the droplet. In the case of spherical squirmers and droplets (not displayed in figure 1*c*), $r_{maj,k} = r_{min,k}$. The fluid phases inside and outside the droplet have dynamic viscosities μ_1 and μ_2, respectively, and the squirmer and droplet propel with speeds U_S and U_D, respectively. Following Reigh *et al.* (2017), we assume that the droplet does not deform. This assumption is reasonable for spherically shaped droplets with sufficiently large surface tension, or for spheroidal droplets covered with shape-preserving surfactants and/or contaminants (Wall *et al.* 2017; Glushkova *et al.* 2023). Indeed, the contaminants give rise to surface viscosities that influence the surface dilatation and surface deformation of the droplet. The resulting forces act to stabilize the droplet's shape (Nganguia *et al.* 2023).

The squirmer's surface velocity consists of radial and tangential modes. In the case of a spherical squirmer (Lighthill 1952; Blake 1971; Pedley 2016),

$$\tilde{\boldsymbol{u}}_{sq} = \sum_{n=0}^{\infty} A_n P_n(\cos\theta)\, \boldsymbol{e}_r + \sum_{n=1}^{\infty} B_n V_n(\cos\theta)\, \boldsymbol{e}_\theta, \tag{2.1}$$

where $(\tilde{})$ denotes a dimensional variable, $P_n(\cos\theta)$ are the Legendre polynomials, $V_n(\cos\theta) = -2P_n^1(\cos\theta)/[n(n+1)]$, $P_n^1(\cos\theta)$ are the associated Legendre polynomials of the first kind, and A_n and B_n are radial and tangential swimming modes, respectively. In the study of squirming microorganisms, it is customary to focus on the tangential modes.

Furthermore, only the first two tangential modes ($B_n = 0$ for $n > 2$) are generally considered, since they help differentiate between various types of squirmers (such as neutral squirmers, pullers and pushers). However, we note that the interpretation and contribution of the tangential swimming modes B_n to the propulsion speed and flow fields depend on the shape of the squirmer, as has been established by Pohnl *et al.* (2020). The propulsion speeds of a translating microorganism in an unbounded Newtonian fluid $U_N = 2B_1/3$ (Lighthill 1952; Blake 1971) and heterogeneous medium $U_B = 6(1 + \delta)B_1/(9 + 9\delta + \delta^2)$ (Nganguia & Pak 2018) depend only on the first actuation mode B_1. Since our focus is on changes in the propulsion speeds, we keep only the first modes A_1 and B_1 in the surface velocity (2.1).

2.1. *The Stokes–Brinkman model*

We extend the Stokes–Brinkman (N-B) model from our previous study (Nganguia *et al.* 2020*a*) to account for the motion of the droplet. The Newtonian region ($r_{maj,s} < r < r_{maj,d}$) is modelled as a purely viscous fluid governed by the incompressible Stokes equation

$$\tilde{\boldsymbol{\nabla}}\tilde{p}_1 + \mu_1\tilde{\boldsymbol{\nabla}} \times \left(\tilde{\boldsymbol{\nabla}} \times \tilde{\boldsymbol{u}}_1\right) = \boldsymbol{0}, \tag{2.2}$$

whereas the heterogeneous medium is governed by the Brinkman equations (Brinkman 1949)

$$-\tilde{\boldsymbol{\nabla}}\tilde{p}_2 + \mu_2\tilde{\nabla}^2\tilde{\boldsymbol{u}}_2 - \mu_2\omega^2\tilde{\boldsymbol{u}}_2 = \boldsymbol{0}, \quad \tilde{\boldsymbol{\nabla}} \cdot \tilde{\boldsymbol{u}}_2 = 0. \tag{2.3a,b}$$

To non-dimensionalize the problem, we scale the velocities using the first mode B_1, lengths using the squirmer's semi-major axis $r_{maj,s}$ and pressure using $\mu_2 B_1/r_{maj,s}$. In dimensionless form, the Stokes equation in the Newtonian domain ($1 < r < b$) becomes

$$\boldsymbol{\nabla}p_1 + \lambda\boldsymbol{\nabla} \times (\boldsymbol{\nabla} \times \boldsymbol{u}_1) = \boldsymbol{0}, \tag{2.4}$$

where the ratio of semi-major axes $b = r_{maj,d}/r_{maj,s}$ is the dimensionless droplet size that represents the size of the Newtonian domain, and $\lambda = \mu_1/\mu_2$ is the viscosity ratio. Similarly, the dimensionless Brinkman equations in the heterogeneous domain ($r > b$) is given by

$$-\boldsymbol{\nabla}p_2 + \nabla^2\boldsymbol{u}_2 - \delta^2\boldsymbol{u}_2 = \boldsymbol{0}, \quad \boldsymbol{\nabla} \cdot \boldsymbol{u}_2 = 0. \tag{2.5a,b}$$

The governing equations are solved in the laboratory frame using the following boundary conditions. In the far field,

$$\boldsymbol{u}_2\,(r \to \infty) = \boldsymbol{0}, \tag{2.6}$$

while

$$\boldsymbol{u}_1\,(r = 1) = \boldsymbol{U}_S + \boldsymbol{u}_{sq} \tag{2.7}$$

on the squirmer surface. The dimensionless surface velocity $\boldsymbol{u}_{sq} = \alpha\cos\theta\boldsymbol{e}_r + \sin\theta\boldsymbol{e}_\theta$, where $\alpha = A_1/B_1$. The boundary conditions on the droplet surface ($r = b$) are given by

the continuity of normal velocities

$$u_1 = u_2 = U_D \cos\theta, \tag{2.8}$$

tangential velocities

$$v_1 = v_2 \tag{2.9}$$

and tangential components of surface force

$$\lambda \boldsymbol{n} \cdot \boldsymbol{T}_1 \cdot \boldsymbol{t} = \boldsymbol{n} \cdot \boldsymbol{T}_2 \cdot \boldsymbol{t}, \tag{2.10}$$

where $\boldsymbol{T}_j = -p_j \boldsymbol{I} + \dot{\varepsilon}_j$, $\boldsymbol{t}$ and $\dot{\varepsilon}_j = \nabla \boldsymbol{u}_j + (\nabla \boldsymbol{u}_j)^{\mathrm{T}}$ denote the unit tangential vector and rate-of-strain tensor, respectively, and $j = 1, 2$.

2.2. *Analytical solution*

The Stokes velocity $\boldsymbol{u}_1$ is obtained using Lamb's general solutions (Happel & Brenner 1973)

$$u_1 = \sum_{n=0}^{\infty} \left(O_n r^{n+1} + Q_n r^{n-1} + \frac{R_n}{r^n} + \frac{S_n}{r^{n+2}} \right) P_n(\cos\theta), \tag{2.11a}$$

$$v_1 = \sum_{n=1}^{\infty} \left(-\frac{n+3}{2} O_n r^{n+1} - \frac{n+1}{2} Q_n r^{n-1} + \frac{n-2}{2} \frac{R_n}{r^n} + \frac{n}{2} \frac{S_n}{r^{n+2}} \right) V_n(\cos\theta). \tag{2.11b}$$

The components $u_2 = \partial\psi_2/\partial\theta/r^2 \sin\theta$ and $v_2 = -\partial\psi_2/\partial r/r \sin\theta$ of the Brinkman velocity $\boldsymbol{u}_2$ are obtained from the streamfunction (Zlatanovski 1999; Palaniappan 2014; Nganguia & Pak 2018)

$$\psi_2 = \sin\theta \sum_{n=0}^{\infty} F_n(r) P_n^1(\cos\theta), \tag{2.12}$$

where

$$F_n(r) = T_n r^{-n} + Y_n r^{n+1} + \frac{\sqrt{r}}{\delta^2} [Z_n I_{n+1/2}(\delta r) + W_n K_{n+1/2}(\delta r)]. \tag{2.13}$$

Here, $I_{n+1/2}$ and $K_{n+1/2}$ are modified Bessel functions of the first and second kind, respectively; $O_n, Q_n, R_n, S_n, T_n, Y_n, Z_n, W_n$ are coefficients determined by applying the boundary conditions. Note that in order to satisfy the boundary condition in the far field (2.6), the coefficients $Y_n = 0$ and $Z_n = 0$. Henceforth, we omit the index n in the coefficients since we focus on a single-mode squirmer ($n = 1$). The velocity in the Stokes domain becomes

$$u_1 = \left(O r^2 + Q + \frac{R}{r} + \frac{S}{r^3} \right) \cos\theta, \tag{2.14a}$$

$$v_1 = \left(-2O r^2 - Q + \frac{1}{2}\frac{R}{r} + \frac{1}{2}\frac{S}{r^3} \right) \sin\theta, \tag{2.14b}$$

and the corresponding velocity in the Brinkman domain is given by

$$u_2 = \left[\frac{2T}{r^3} + W \frac{\mathrm{e}^{-r\delta}(1 + r\delta)}{\delta^{7/2} r^3} \right] \cos\theta, \tag{2.15a}$$

$$v_2 = \left[\frac{T}{r^3} + W \frac{\mathrm{e}^{-r\delta}(1 + r\delta + r^2\delta^2)}{\delta^{7/2} r^3} \right] \sin\theta. \tag{2.15b}$$

Upon applying boundary conditions, we obtain the system of equations

$$\begin{pmatrix} 1 & 1 & 1 & 1 & 0 & 0 \\ -2 & -1 & -\frac{1}{2} & \frac{1}{2} & 0 & 0 \\ -b^2 & -1 & -\frac{1}{b} & -\frac{1}{b^3} & \frac{2}{b^3} & s_1 \\ b^2 & 1 & \frac{1}{b} & \frac{1}{b^3} & 0 & 0 \\ 2b^2 & 1 & \frac{1}{2b} & -\frac{1}{2b^3} & \frac{1}{b^3} & s_2 \\ 3b & 0 & 0 & \frac{3}{b^4} & -\frac{6}{\lambda b^4} & s_3 \end{pmatrix} \begin{bmatrix} O \\ Q \\ R \\ S \\ T \\ W \end{bmatrix} = \begin{bmatrix} \alpha + U_S \\ 1 - U_S \\ 0 \\ U_D \\ 0 \\ 0 \end{bmatrix}, \tag{2.16}$$

where

$$\left.\begin{aligned} s_1 &= \frac{\sqrt{2\pi}\mathrm{e}^{-b\delta}\sqrt{b\delta}(b\delta+1)}{b^{7/2}\delta^4}, \\ s_2 &= \frac{\sqrt{\frac{\pi}{2}}\mathrm{e}^{-b\delta}\sqrt{b\delta}(b^2\delta^2+b\delta+1)}{b^{7/2}\delta^4}, \\ s_3 &= -\frac{\sqrt{\frac{\pi}{2}}\mathrm{e}^{-b\delta}\sqrt{b\delta}(b\delta(b\delta(b\delta+3)+6)+6)}{b^{9/2}\delta^4\lambda}, \end{aligned}\right\} \tag{2.17}$$

which yields the velocity field coefficients (see Appendix A). For both §§ 3 and 4, we first discuss the propulsion for purely tangential squirming modes ($\alpha = 0$), followed by an analysis of the co-swimming state ($\alpha \neq 0$).

2.3. *Numerical simulations*

The equations are solved numerically using the finite element method implemented in the COMSOL Multiphysics environment. To take advantage of the axial symmetry of the problem, an axisymmetric computational domain in the rz plane is used to simulate only half of the full flow domain. The equation describing the surface of the prolate spheroidal body reads

$$\frac{z^2}{r_{maj}^2} + \frac{r^2}{r_{min}^2} = 1, \tag{2.18}$$

where $r^2 = x^2 + y^2$.

The squirmer and the droplet are modelled as half-prolate spheroids centred at the origin and whose major axes coincide with the axis of symmetry. The semi-major axis of the droplet, $r_{maj,d}$, is scaled with $b > 1$ such that $r_{maj,d} = br_{maj,s}$ to model a range of droplet to squirmer size ratios. Semi-minor axes of both the squirmer and the droplet are calculated based on their respective eccentricities using the definition of eccentricity $e_k = c_k/r_{maj,k}$, where $c_k = (r_{maj,k}^2 - r_{min,k}^2)^{1/2}$. Note that for a spherical shape, $e_k = 0$.

A large computational domain of size $500a_{sq} \times 500a_{sq}$ is employed to ensure negligible confinement effects. Here P1+P1 (first order for fluid velocity and first order for pressure)

triangular mesh elements are used for the simulations, with local mesh refinement near the squirmer and inside the droplet domain to properly resolve the spatial variation of the flow field. The degree of freedom ranges from 1×10^5 to 4×10^5 for the simulations depending on b, which enlarges the finely meshed droplet domain as it gets larger and, therefore, increases the degree of freedom.

The unknown swimming velocity of the squirmer is obtained by solving the momentum and continuity equations simultaneously with the force-free swimming condition applied on the squirmer surface. Solving the fully coupled problem, we obtain the velocity and pressure fields. To find the droplet velocity, we evaluate the flow velocity at the droplet boundary. We used the parallel direct solver (PARDISO) for all simulations. It should be noted here that the numerical simulations compute the instantaneous velocities of the squirmer and the droplet while they are in a concentric configuration.

3. Effects of heterogeneity on propulsion

In this section we only consider the spherical squirmer and droplet. We substitute the velocity fields $\boldsymbol{u}_j$ into the force-free conditions

$$\int_{\Gamma_1} \boldsymbol{T}_1 \cdot \boldsymbol{n}\, \mathrm{d}\Gamma_1 = \boldsymbol{0}, \quad \int_{\Gamma_2} \boldsymbol{T}_2 \cdot \boldsymbol{n}\, \mathrm{d}\Gamma_2 = \boldsymbol{0}, \tag{3.1a,b}$$

to determine the unknown swimming speeds of the squirmer U_S and droplet U_D. Here, Γ_1 and Γ_2 denote the squirmer and droplet interfaces, respectively. The swimming speed of the squirmer is given by

$$U_S = \frac{1}{3\mathcal{B}} \Big\{ (b-1)^2(3+6b+4b^2+2b^3)(18+18b\delta+3b^2\delta^2+b^3\delta^3) \\ +6[-9-9b\delta+15b^2+9b^5+(15b^3+9b^6)\delta+(b^7-b^2)\delta^2]\lambda \Big\}, \tag{3.2}$$

and the swimming speed of the droplet is given by

$$U_D = \frac{30b^2\,(1+b\delta)\,\lambda}{\mathcal{B}}, \tag{3.3}$$

where

$$\mathcal{B} = (b^5-1)(18+18b\delta+3b^2\delta^2+b^3\delta^3) + (2+3b^5)(9+9b\delta+b^2\delta^2)\lambda. \tag{3.4}$$

In the presence of the dimensionless radial mode α, the squirmer speed becomes

$$U_S = \frac{1}{\mathcal{B}_\alpha} \Big\{ \frac{1}{\mathcal{B}} [90\lambda b^2(\alpha+1)(\delta b+1)[5\delta(b^6-b^3)+9b^5-5b^3+\lambda(6b^5+4)-4]] \\ -2[(\alpha-2)\delta b^6+5(\alpha+1)\delta b^3-3b(2\alpha\delta+\delta)+3(\alpha-2)(\lambda+1)b^5 \\ +3(2\alpha+1)(2\lambda-3)+15(\alpha+1)b^2] \Big\}, \tag{3.5}$$

where

$$\mathcal{B}_\alpha = 6[(b^5-1)(\delta b+3)+\lambda(3b^5+2)], \tag{3.6}$$

and the droplet speed is given by

$$U_D = \frac{30(\alpha+1)\lambda b^2(\delta b+1)}{\mathcal{B}}. \tag{3.7}$$

By setting (3.5) equal to (3.7) ($U_S = U_D$), we obtain the ratio α_{SD} necessary for the squirmer and droplet to move at the same speeds,

$$\alpha_{SD} = \frac{1}{\mathcal{B}_{SD}}[(b-1)^2(3+6b+4b^2+2b^3)(18+18b\delta+3b^2\delta^2+b^3\delta^3) + 6(b^5-1)(9+9b\delta+b^2\delta^2)\lambda], \tag{3.8}$$

where

$$\mathcal{B}_{SD} = (b^5+5b^2-6)(18+18b\delta+3b^2\delta^2+b^3\delta^3)+3(b^5+4)(9+9b\delta+b^2\delta^2)\lambda. \tag{3.9}$$

Substituting α_{SD} into (3.5) or (3.7) yields the co-swimming speed

$$U_{SD} = \frac{90b^2\,(1+b\delta)\,\lambda}{\mathcal{B}_{SD}}. \tag{3.10}$$

3.1. *Validation*

We validate our analytical model and numerical implementation against the results in Reigh *et al.* (2017), where the set-up consists of an encapsulated squirmer in a homogeneous Newtonian fluid ($\delta = 0$). In the limit of $\delta \to 0$, the propulsion speeds in (3.2) and (3.3) reduce to

$$U_S = \frac{2[3+5b^2(\lambda-1)-3\lambda+b^5(2+3\lambda)]}{6(\lambda-1)+b^5(6+9\lambda)} \tag{3.11}$$

and

$$U_D = \frac{10b^2\lambda}{6(\lambda-1)+b^5(6+9\lambda)}. \tag{3.12}$$

These equations are identical to those in Reigh *et al.* (2017, (19)) after letting $\lambda = 1/\tilde{\lambda}$, where $\tilde{\lambda}$ is the viscosity ratio in their paper. Figure 2(*a*) shows the propulsion speed of the squirmer, while figure 2(*b*) shows the ratio of the droplet to squirmer speeds as a function of the droplet size b with $\delta = 10^{-3}$. The dashed curves denote the results using the purely viscous system in Reigh *et al.* (2017), the solid curves are obtained from (3.11) and (3.12), and the symbols denote numerical simulations. Similarly, for the co-swimming state (figure 2*c*), the propulsion speed in (3.10) reduces to

$$U_{SD} = \frac{90\lambda b^2}{18(b^5+5b^2-6)+27(b^5+4)\lambda}, \tag{3.13}$$

which, in the limit $\delta \to 0$, is identical to the equation provided in (Reigh *et al.* 2017, (28)).

To further validate the numerical implementation of the Brinkman equations and the effects of the fluid resistance δ, we consider the flow decay. Figure 3 shows the magnitude of the velocity $\|\boldsymbol{u}_1 + \boldsymbol{u}_2\|$ as a function of the distance from the squirmer's surface ($r = 1$) with $b = 1.025$ and $\lambda = 10$. The velocity magnitude is plotted for $\theta = 0$ (figure 3*a*) and $\theta = \pi/2$ (figure 3*b*). The flow decays as $1/r^3$ in the far field (Nganguia & Pak 2018), and we found excellent agreement between our analytical model (solid lines) and numerical simulations (symbols) for values of the fluid resistance $\delta = 10^{-3}$, 1, 10.

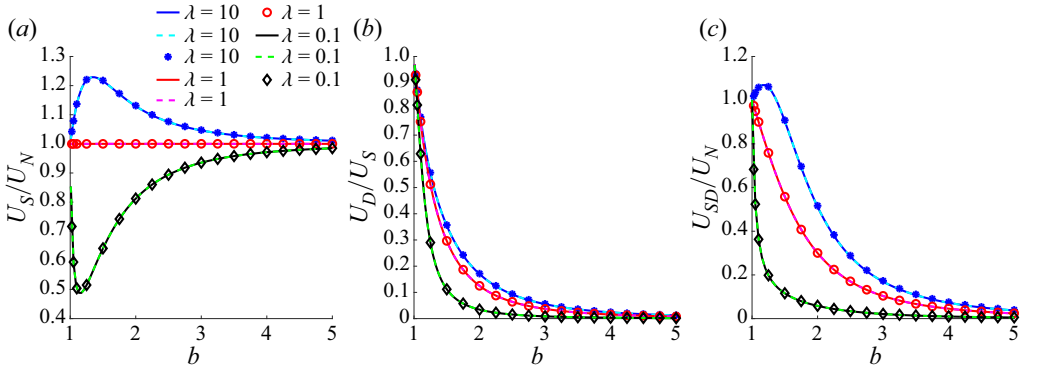

Figure 2. (*a*) Propulsion speed for the squirmer, (*b*) ratio of the droplet to squirmer speeds, and (*c*) propulsion speed for the co-swimming state ($U_{SD} = U_S = U_D$) as a function of the droplet size b. In (*a*,*c*) the speeds are scaled by $U_N = 2/3$, the propulsion speed of a squirmer in an unbounded Newtonian fluid. The dashed curves denote the results using the purely viscous system (see Reigh *et al.* (2017), (10) and (11)), the solid curves are obtained from the N-B model ((3.11) and (3.12)), and the symbols denote numerical simulations. The fluid resistance $\delta = 10^{-3}$ for the N-B model and the numerical simulations.

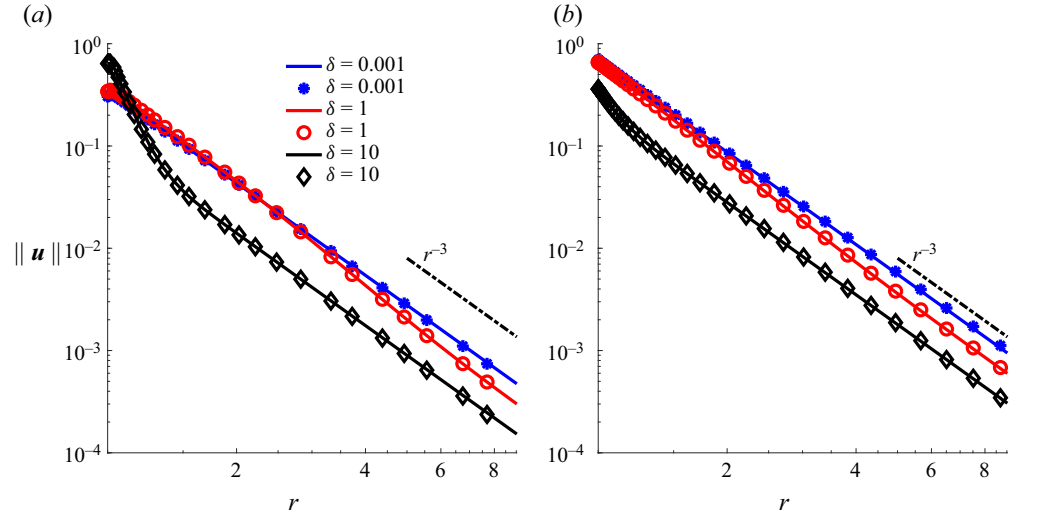

Figure 3. Velocity magnitude $\|\boldsymbol{u}\| = \sqrt{u^2 + v^2}$ as a function of the distance from the squirmer's surface for (*a*) $\theta = 0$ and (*b*) $\theta\pi/2$. In both panels, $b = 1.025$ and $\lambda = 10$. The solid curves are obtained from the N-B model and the symbols denote numerical simulations.

3.2. *Effects of fluid resistance on the propulsion speed of the squirmer ($\alpha = 0$)*

We now investigate the effects of the fluid resistance δ on the propulsion speed of the squirmer. We focus on the squirmer since our results show that the squirmer's speed exhibits the most interesting variations. As the heterogeneous medium becomes more resistant to fluid motion ($\delta \to \infty$), the droplet's speed is completely suppressed (refer to Appendix B) while the squirmer continues propelling. This configuration is akin to restricting motile organisms in a static droplet to, for instance, investigate the dynamics of organism-surface interactions (Raveshi *et al.* 2021). Also note that throughout this section,

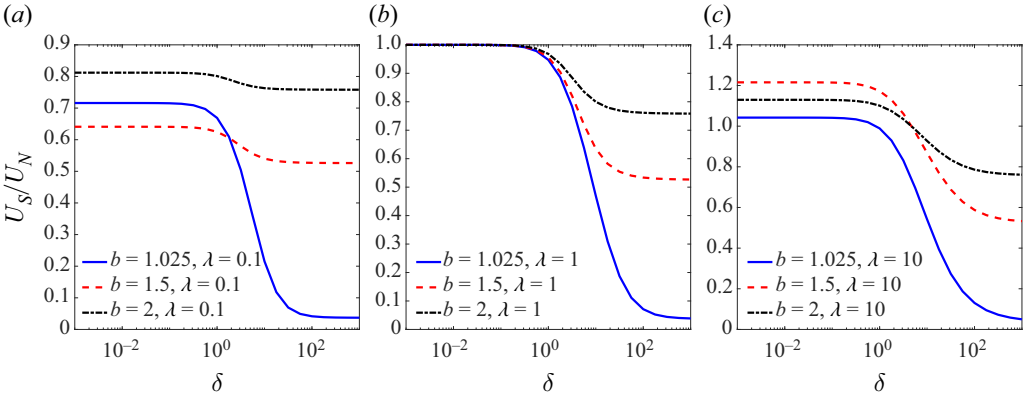

Figure 4. Propulsion speed for the squirmer as a function of fluid resistance δ. In all panels, the speed is scaled by $U_N = 2/3$, the propulsion speed of a squirmer in an unbounded domain in a Newtonian fluid. The solid curves are obtained from (3.2).

and unless otherwise noted, we compare the squirmer speed to that of a squirmer in an unbounded Newtonian fluid.

Figure 4 shows the propulsion speed scaled with U_N as a function of the fluid resistance δ. Taken together, for all values of the viscosity contrast and across the range of fluid resistance, the squirmer is always able to move in its enclosure. Moreover, we note a non-trivial dynamics that depends on the viscosity ratio λ and droplet size b. Figure 4(a) shows the speed for $\lambda = 0.1$. In this case, the squirmer always moves slower than its unbounded counterpart. However, speed enhancement can be achieved relative to the droplet size. Comparing the curves in the range $\delta \lessapprox 1$, we observe that the speed is non-monotonic: as b increases, the squirmer's speed first decreases before increasing after reaching a minimum. On the other end when $\delta > 1$, the speed monotonically increases with a larger droplet size. The increase in the speed is not unexpected: as $b \to \infty$, the problem becomes identical to a squirmer in an unbounded Newtonian fluid.

When $\lambda = 1$ (figure 4b), the squirmer speed is much the same as that experienced by a squirmer in a Newtonian pocket in a heterogeneous medium (Nganguia & Pak 2018). Up to $\delta \approx 1$, the squirmer swims at the same speed experienced by a squirmer in an unbounded Newtonian fluid. The speed then decreases monotonically to a non-zero value. The magnitude of the speed as $\delta \to \infty$ is determined by the droplet size. Here, as in the case of a lower viscosity ratio, increasing b has the effect of raising the squirmer's speed. For $\lambda = 10$ and fluid resistance up to $\delta \approx 1$ (for $b = 1.025$) or $\delta \approx 7$ (for $b \geq 1.5$), the squirmer always moves faster compared with a squirmer in an unbounded Newtonian fluid (as illustrated in figure 4c). Similarly to the case with a lower viscosity ratio, the speed varies non-monotonically with the droplet size. This time, as b increases, the squirmer's speed reaches a maximum speed $U_S/U_N \approx 1.2$ ($b = 1.5$). For larger values of the fluid resistance, the speeds asymptote to non-zero values, meaning the squirmer is always able to move albeit at a slower speed than that of a squirmer in an unbounded Newtonian fluid. For targeted drug delivery, it is advantageous that the squirmer and droplet move at the same speed as much as possible. A sufficient condition to attain this state is to account for the first radial swimming modes A_1 (Reigh *et al.* 2017) in the squirmer's surface velocity $\boldsymbol{u}_{sq}$ (2.1). Since the droplet propels in a heterogenous medium, one may ponder, naturally: How do the radial swimming mode and the co-swimming speed depend on the fluid resistance?

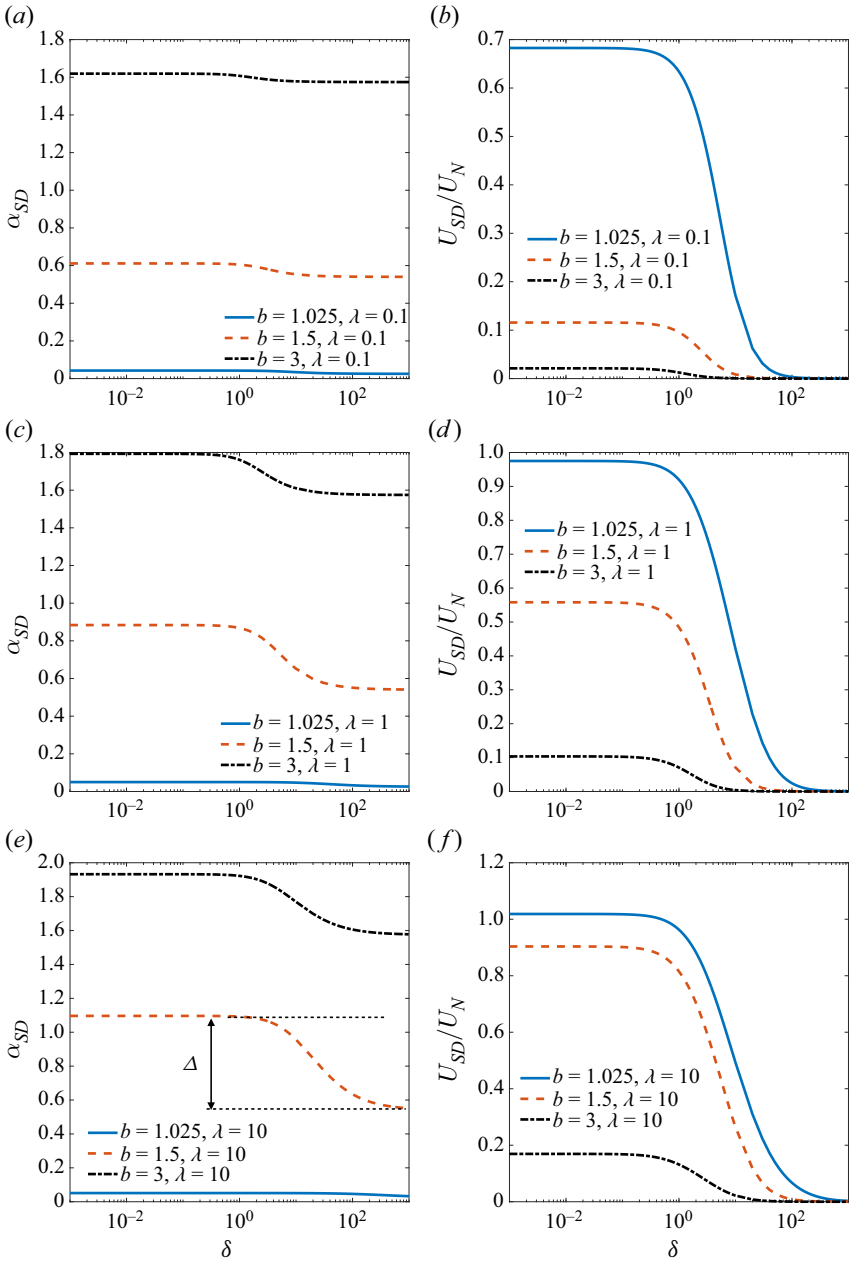

Figure 5. Modes ratio α_{SD} (*a*,*c*,*e*) and co-swimming speed U_{SD}/U_N (*b*,*d*,*f*) for the co-swimming state as a function of the fluid resistance δ. The values of the viscosity ratio are $\lambda = 0.1$ (*a*,*b*), $\lambda = 1$ (*c*,*d*) and $\lambda = 10$ (*e*,*f*). The solid, dashed and dash-dotted curves represent values of the droplet size $b = 1.025, 1.5, 3$, respectively.

3.3. *Dependence of the co-swimming variables on the fluid resistance ($\alpha \neq 0$)*

To answer the previous question, we must analyse the dependence of the co-swimming mode ratio α_{SD} (3.8) on the fluid resistance δ. This dependence is illustrated in figure 5 for viscosity ratios $\lambda = 0.1$ (*a*), $\lambda = 1$ (*c*) and $\lambda = 10$ (*e*). In all three panels, α_{SD} reveals

two distinct regions of near-constant values: one at low fluid resistance and another at high fluid resistance. A transition region Δ stretches across the interval $\delta \in [1, 100]$. We observe that α_{SD} is larger for low δ compared with the smaller values at large δ. The magnitude of the transition phase shows a non-monotonic dependence on the droplet size b: the difference between α_{SD} at small and large δ is such that it first increases with b up to ≈ 1.5, then asymptote to a non-zero lower value. These changes are more clearly observed at a high viscosity contrast (figure 5*e*). Physically, we can deduce that the radial mode is less effective at large fluid resistance. The co-swimming speed U_{SD} is shown in figure 5(*b*,*d*,*f*). Taken together, they show that the squirmer-droplet system is fastest at low values of the droplet size and low fluid resistance. The maximum value of the propulsion speed reduces monotonically with increasing b. Moreover, U_{SD} also depends on the viscosity contrast λ. For $\lambda = 10$, the system moves at least as fast as a squirmer in an unbounded Newtonian fluid ($U_{SD} \gtrapprox 1$) with the maximum speed occurring at low b and δ. As the viscosity contrast λ decreases (from 10 to 0.1), so does the propulsion speed and the system now propels more slowly compared with a squirmer in an unbounded Newtonian fluid.

4. Effects of squirmer and droplet shapes on propulsion

Studies have shown that spheroidal microorganisms in Newtonian fluids generally swim faster compared with their spherical counterparts (Keller & Wu 1977; Theers *et al.* 2016; Pohnl *et al.* 2020; Guo *et al.* 2021), with a propulsion speed given by $U_N = \tau_0[\tau_0 - (\tau^2 - 1)\coth^{-1}\tau_0]$, where the surface of the spheroid $\tau_0 = 1/e$ and e is the eccentricity of the squirmer. The gain in speed due to the spheroidal shape, however, depends on the fluid in which the squirmer moves. For instance, a spheroidal neutral squirmer in a shear-thinning fluid propels more slowly for $e \lessapprox 0.85$ and faster for $e > 0.85$ (van Gogh *et al.* 2022). In this section we consider various shape configurations for the squirmer and droplet. While the surface velocity given in (2.1) is adequate for spherically shaped organisms, a more general surface velocity for spheroidal squirmers was proposed by Keller & Wu (1977). The surface velocity was also formulated in terms of the prolate spheroidal coordinate system (τ, ζ, ϕ) for a single- and two-mode squirmer (Theers *et al.* 2016; Pohnl *et al.* 2020; van Gogh *et al.* 2022), where $1 \leq \tau \leq \infty$, $-1 \leq \zeta \leq 1$ and $0 \leq \phi \leq 2\pi$. Since previous studies of spheroidal squirmers did not provide a general form of the radial modes, we propose the expression

$$\tilde{\boldsymbol{u}}_{sq} \cdot \boldsymbol{e}_\tau = \tau_0^2(\tau_0^2 - 1)^{-1/2}(\tau_0^2 - \zeta^2)^{-1/2} \sum_{n\geq 0} A_n P_n(\zeta) \tag{4.1}$$

for the radial component of the surface velocity. Note that in the limit $\tau_0 \to \infty$, the term $\tau_0^2(\tau_0^2 - 1)^{-1/2}(\tau_0^2 - \zeta^2)^{-1/2}P_n(\zeta) \to P_n(\zeta)$ and $\zeta \to \cos\theta$. It follows that in this limit, (4.1) converges to $A_n P_n(\cos\theta)\boldsymbol{e}_r$, and the expression is matched identically to the surface velocity of a spherical squirmer (Lighthill 1952; Blake 1971). Thus, for the spheroidal neutral squirmer considered in the present study, the surface velocity (3.1*a*,*b*) becomes

$$\tilde{\boldsymbol{u}}_{sq} = A_1 \zeta \tau_0^2(\tau_0^2 - 1)^{-1/2}(\tau_0^2 - \zeta^2)^{-1/2}\boldsymbol{e}_\tau - B_1 \tau_0(1 - \zeta^2)^{1/2}(\tau_0^2 - \zeta^2)^{-1/2}\boldsymbol{e}_\zeta. \tag{4.2}$$

In what follows, we again focus on the squirmer's speeds U_S and U_{SD} and leave the discussion of the droplet's speed to Appendix B. We consider the squirmer's eccentricities e_s up to 0.9 (corresponding to ciliates with an aspect ratio of 2 (Rodrigues *et al.* 2021)), as well as the droplet's eccentricities $e_d \leq 0.9$.

4.1. *Effects of shapes on the propulsion speed of the squirmer ($\alpha = 0$)*

We numerically investigate the effects of various squirmer-droplet shape combinations on the swimming dynamics in a Newtonian fluid ($\delta = 10^{-3}$). We consider three cases: S1, a spherical squirmer in a spheroidal droplet; S2, a spheroidal squirmer in a spherical droplet; and S3, a spheroidal squirmer in a spheroidal droplet. Figure 6(*a*,*b*) shows the propulsion speed of a spherical squirmer in a spheroidal droplet (system S1) as a function of the droplet size b. Compared with an unbounded spherical squirmer, the squirmer enclosed in the droplet can move significantly slower (up to 50 % reduction for $\lambda = 0.1$) or faster (more than 20 % enhancement for $\lambda = 10$) at low values of the droplet size ($b < 2.5$). We also note that the propulsion speed is higher for a droplet with lower eccentricity, as illustrated by the dashed curves ($e_d = 0.3$) versus the solid curves ($e_d = 0.9$). This shape effect becomes much less pronounced for $b > 2.5$, as the squirmer's propulsion speeds converge to that of their unbounded counterparts.

A spheroidal squirmer in a spherical droplet (S2, figure 6*c*,*d*) displays similar features in comparison to S1. The squirmer has slower propulsion speed for $\lambda = 0.1$, while it propels faster at $\lambda = 10$, compared with unbounded spheroidal squirmers. However, two important features distinguish S1 from S2. First, in S2 with $\lambda = 0.1$, the spheroidal squirmer with higher eccentricity $e_s = 0.9$ propels significantly faster compared with the squirmer with $e_s = 0.3$, while the inverse holds true for $\lambda = 10$: higher eccentricity yields lower propulsion speed. Second, in both figures 6(*c*) and 6(*d*), the shape effects are pronounced for a wider range of domain sizes (at $b = 5$, one can visibly note a difference between the speeds resulting from $e_s = 0.3$ and $e_s = 0.9$).

These shape effects from S2 are also observed in S3, where both the squirmer and droplet have spheroidal shapes (figure 6*e*,*f*). In other words, comparing S2 and S3, the eccentricity of the droplet does not appear to have a large influence on the propulsion of the spheroidal squirmer. We note, however, that the maximum gain in propulsion speed ($\lambda = 10$, figure 6*f*) between a spheroidal squirmer in a more elongated droplet ($e_s = 0.3$, $e_d = 0.9$) and spheroidal squirmer in a lesser elongated droplet ($e_s = 0.9$, $e_d = 0.3$) is of the same order of magnitude: about a 16 % gain compared with unbounded spheroidal squirmers. It is worth noting that our results show all three systems (S1, S2 and S3) yield identical behaviours when $\lambda = 1$. The difference in propulsion speeds between the squirmers in these respective systems and those in unbounded domains is less than 0.1 %. This suggests that the viscosity contrast can be an effective tool to control the dynamic behaviour of a caged squirmer, providing more options to design micro-robots for drug delivery systems.

4.2. *Effects of shapes on the co-swimming variables ($\alpha \neq 0$)*

For locomotion in an unbounded Newtonian fluid, the radial mode was found to play a diminishing role for spheroidal squirmers (Keller & Wu 1977). Thus, it is natural to ponder whether the radial mode still enables co-swimming for the systems we discussed in the previous section. We first consider systems S1 and S2, where both spherical and spheroidal shapes are involved. For a fixed eccentricity, we determine the values, when they exist, of the radial mode at which co-swimming ($U_{SD} = U_S = U_D$) is achieved. Figure 7 shows the mode ratio α_{SD} as a function of the eccentricity of the squirmer (*a*–*c*; with a spherical droplet) or droplet (*d*–*f*; with a spherical squirmer). In each panel, the solid, dashed and dash-dotted curves represent values of the droplet size $b = 1.5, 2.5, 3.5$, respectively. The viscosity ratios are $\lambda = 0.1$ (figure 7*a*,*d*), $\lambda = 1$ (figure 7*b*,*e*) and $\lambda = 10$ (figure 7*c*,*f*).

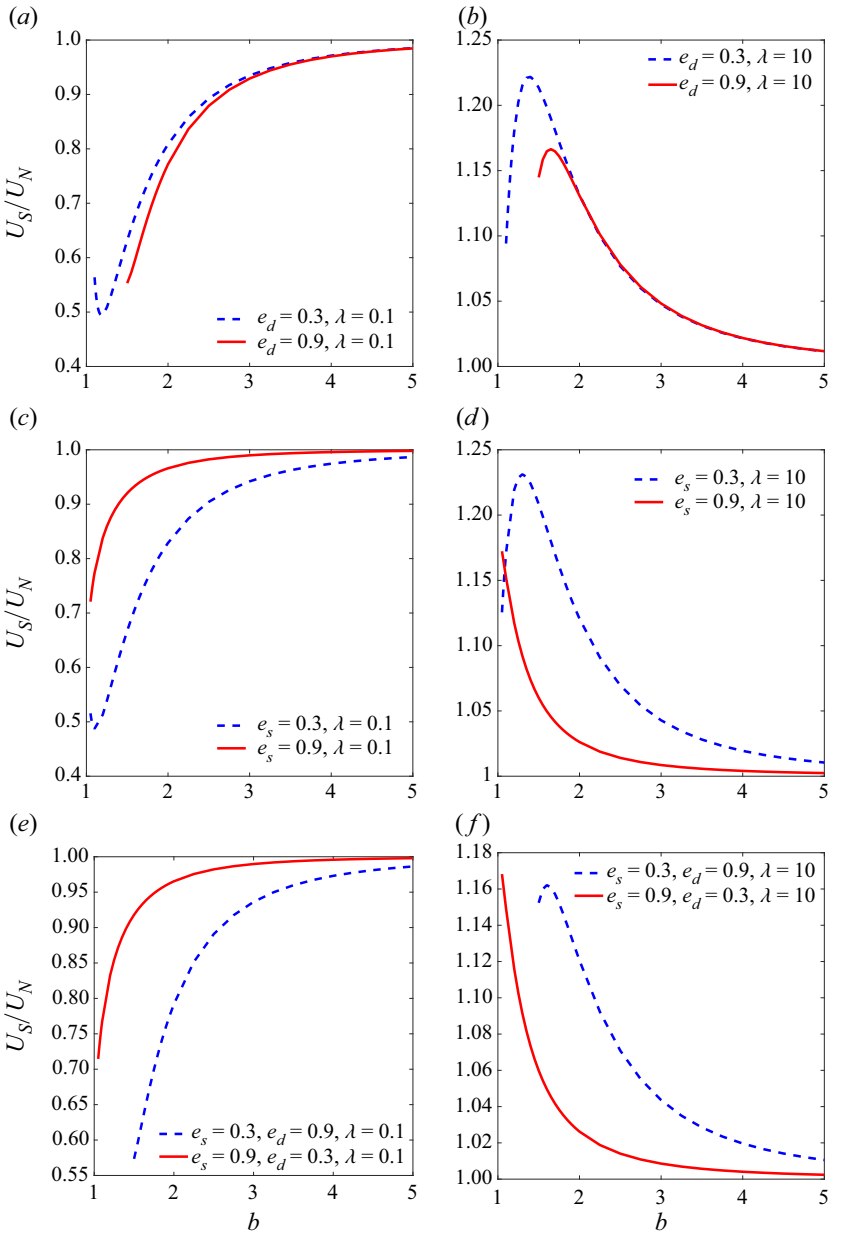

Figure 6. Propulsion speed for the spherical squirmer in a spheroidal droplet (*a*,*b*), the spheroidal squirmer in a spherical droplet (*c*,*d*) and the spheroidal squirmer in a spheroidal droplet (*e*,*f*) as a function of droplet size b. Here $\lambda = 0.1$ for panels in the left column and $\lambda = 10$ for panels in the right column. All speeds are scaled by $U_N = 2/3$, the propulsion speed of a spherical squirmer in an unbounded domain in a Newtonian fluid, or by $U_N = \tau_0[\tau_0 - (\tau_0^2 - 1)\coth^{-1}\tau_0]$, the propulsion speed of a spheroidal squirmer in an unbounded domain in a Newtonian fluid.

In the case of a spheroidal squirmer in a spherical droplet with $\lambda \geq 1$ (figure 7*b*,*c*), α_{SD} decreases with increasing eccentricity. This suggests that the radial mode has less influence on the propulsion speed of a spheroidal squirmer, and is in qualitative agreement with predictions for an unbounded spheroidal squirmer. The droplet size also factors in the

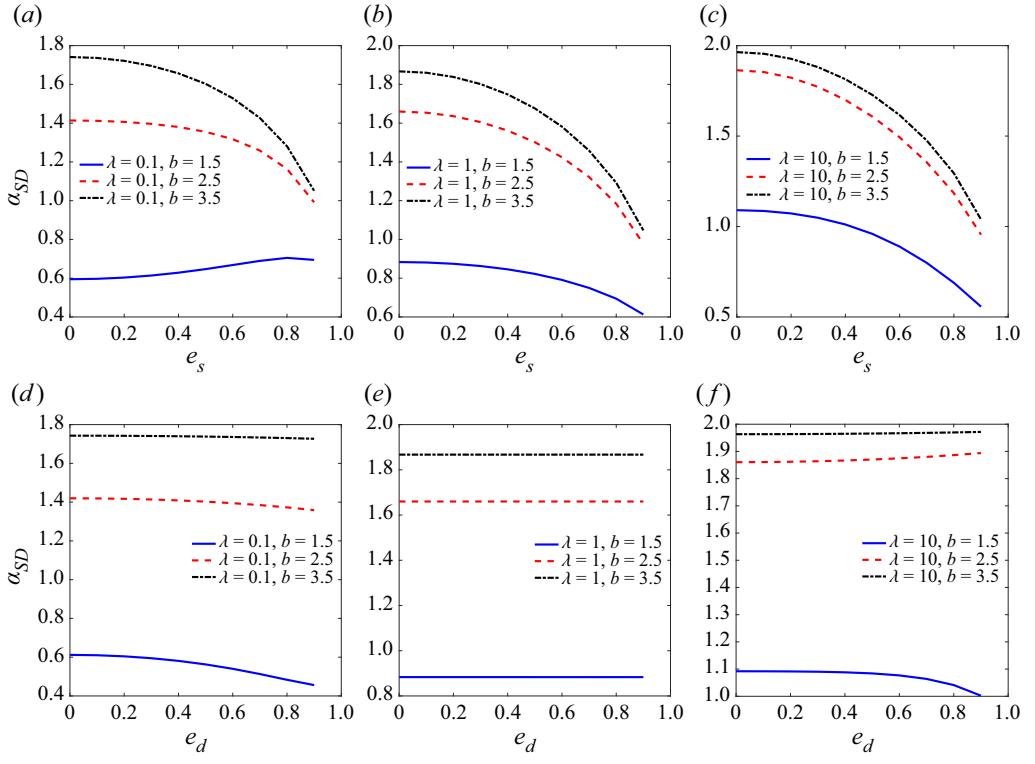

Figure 7. Mode ratio α_{SD} as a function of the eccentricity for (*a–c*) a spheroidal squirmer in a spherical droplet and (*d–f*) a spherical squirmer in a spheroidal droplet. The fluid outside the droplet is Newtonian ($\delta = 10^{-3}$).

observed trend: increasing b yields larger values of α_{SD}. For $\lambda < 1$ (figure 7*a*), we observe the same dependence on b. However, for small b, increasing the eccentricity also increases α_{SD} (albeit not significantly), while it decreases α_{SD} for larger b.

Our results also show an increase in the radial mode with increasing droplet size for a spherical squirmer in a spheroidal droplet. However, when comparing with the spheroidal squirmer in a spherical droplet, we observe a few trends that are reversed with more moderate variations over the range of eccentricities. At $b \leq 2.5$, the radial mode necessary to achieve co-swimming now decreases for $\lambda < 1$ (figure 7*d*), or remains constant for $\lambda = 1$ (figure 7*e*). For $\lambda > 1$ (figure 7*f*), the radial mode shows a strong dependence on the droplet size: α_{SD} decreases with increasing e for $b < 2$, and increases for $b \in (2, 3.5]$. As $b \gg 3.5$, the radial mode decouples from the eccentricity.

The propulsion speeds corresponding to the mode ratios in figure 7 are shown in figure 8. Taking all the panels together, we observe a number of features: (1) the co-swimming speed is always smaller compared with the speed of an unbounded squirmer, (2) increasing the viscosity contrast also increases the propulsion speed, and (3) smaller droplet radii yield the largest gain in speed. The influence of eccentricity is more pronounced for a spheroidal squirmer in a spherical droplet, with reduced effects at larger droplet radii (figure 8*a–c*). For a spherical squirmer in a spheroidal droplet, our results show that the speed is independent of the droplet's eccentricity for $b > 1.5$, as illustrated by the near-constant curves in figure 8(*d–f*). High eccentricity shows a modest increase of the propulsion speed for $\lambda = 0.1$ (figure 8*d*), and a more gradual decrease across the range of eccentricities for $\lambda = 10$ (figure 8*f*).

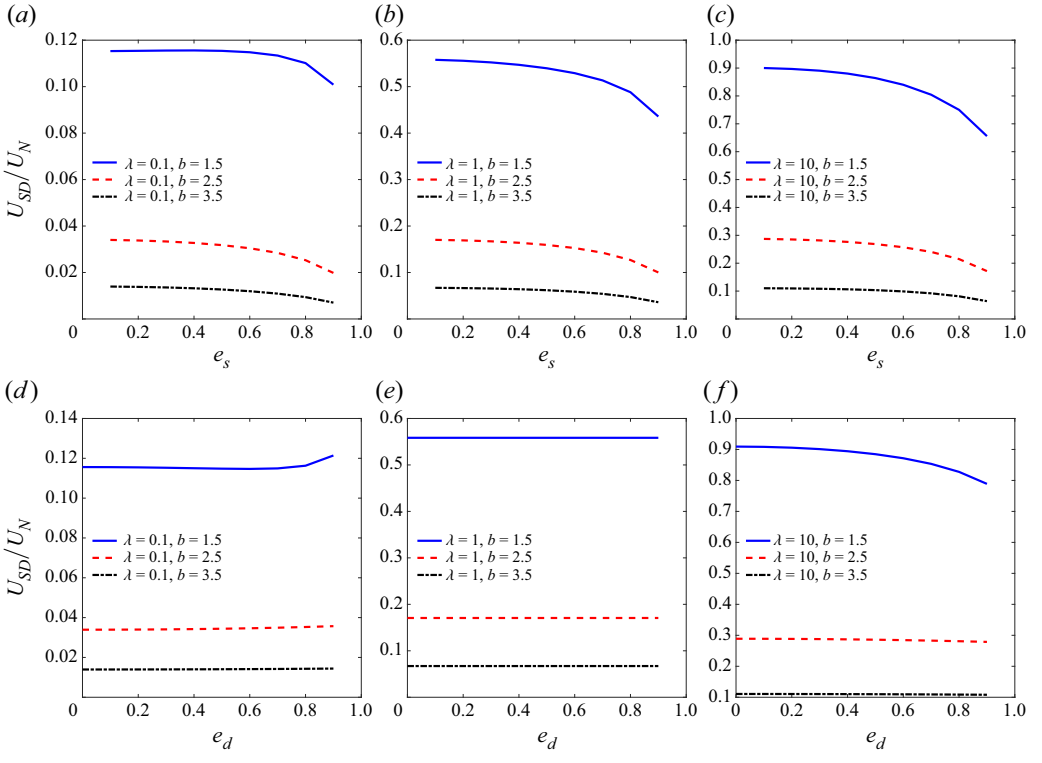

Figure 8. Co-swimming propulsion speed U_{SD} as a function of the eccentricity for (*a–c*) a spheroidal squirmer in a spherical droplet and (*d–f*) a spherical squirmer in a spheroidal droplet. All speeds are scaled by $U_N = 2/3$, the propulsion speed of a spherical squirmer in an unbounded domain in a Newtonian fluid, or by $U_N = \tau_0[\tau_0 - (\tau_0^2 - 1)\coth^{-1}\tau_0]$, the propulsion speed of a spheroidal squirmer in an unbounded domain in a Newtonian fluid. The fluid outside the droplet is Newtonian ($\delta = 10^{-3}$).

Next, we investigate the mode ratio and propulsion speed for system S3: a spheroidal squirmer in a spheroidal droplet. We consider droplets at low eccentricity ($e_d = 0.3$, figure 9*a*,*b*) and high eccentricity ($e_d = 0.9$, figure 9*c*,*d*), and plot the mode ratio α_{SD} (figure 9*a*,*c*) and the co-swimming speed U_{SD}/U_N (figure 9*b*,*d*) as a function of the droplet size b.

First, for $b \gg 1$, the mode ratio α_{SD} decreases quite significantly with increasing the squirmer's eccentricity e_s. Again, this suggests that the radial mode has a reduced influence for elongated squirmers, consistent with the predictions in Keller & Wu (1977). Second, for a fixed e_s, α_{SD} increases monotonically and appears to asymptote as $b \to \infty$ (unbounded domain). In this limit, the mode ratio no longer varies with the viscosity ratio. The effects of the viscosity ratio on α_{SD} are more significant at moderate b, and also more pronounced for squirmers with lower eccentricity. In this regime, increasing λ leads to an increase (decrease) in α_{SD} for $e_s = 0.3$ ($e_s = 0.9$).

Similarly, we can observe a few patterns regarding the spheroidal squirmer's speed (which coincides with the co-swimming speed) in figure 9(*b*,*d*). For $b \gg 1$, the speed decreases monotonically and asymptotes to values near zero. This suggests that while the squirmer is always able to propel, its speed is significantly affected by the shape of the domain in which it moves (in the present case, a spheroidal domain). The observation contrasts with propulsion in an unbounded domain (Theers *et al.* 2016;

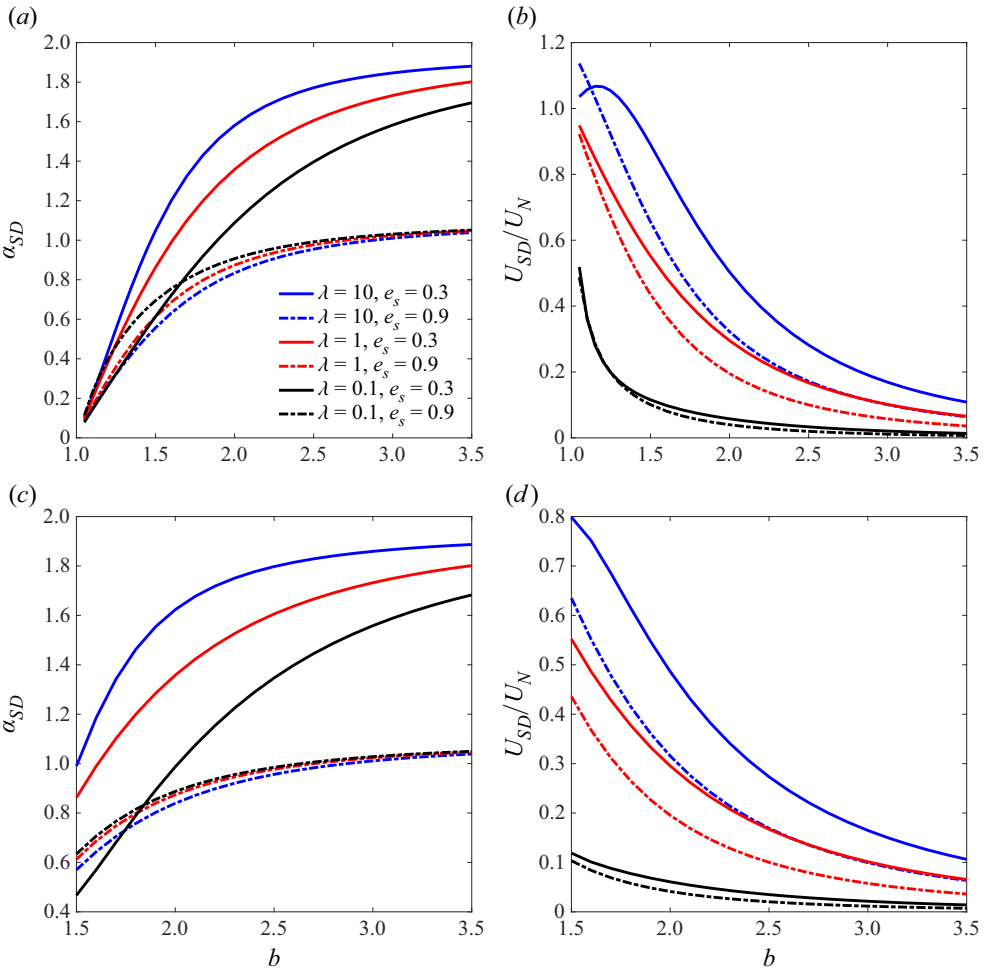

Figure 9. (*a*,*c*) Mode ratio and (*b*,*d*) co-swimming propulsion speed for the spheroidal squirmer in a spheroidal droplet as a function of droplet size b. The droplet's eccentricities are (*a*,*b*) $e_d = 0.3$ and (*c*,*d*) $e_d = 0.9$. The curves denote the values of the squirmer's eccentricities $e_s = 0.3$ (solid) and $e_s = 0.9$ (dotted), while the colours differentiate between viscosity ratios: blue for $\lambda = 10$, red for $\lambda = 1$ and black for $\lambda = 0.1$. In (*b*,*d*) the propulsion speed is scaled with $U_N = \tau_0[\tau_0 - (\tau_0^2 - 1)\coth^{-1}\tau_0]$, the propulsion speed of a spheroidal squirmer in an unbounded Newtonian fluid.

Pohnl *et al.* 2020), where the spheroidal squirmer's speed is greater than 2/3 (the speed of an unbounded spherical squirmer). The eccentricity of the enclosing spheroidal domain (the droplet) further influences the co-swimming speed, which decreases with increasing e_d. For instance, $U_{SD}/U_N \approx 0.9$ with $b = 1.5$ and $\lambda = 10$ at $e_d = 0.3$ (figure 9*b*), whereas $U_{SD}/U_N = 0.8$ at $e_d = 0.9$ (figure 9*d*). The difference in speed between the droplet's eccentricities becomes less pronounced for a fixed λ as $b \to \infty$, and the speeds are nearly identical for the full range of b for a small viscosity contrast (here, for $\lambda = 0.1$).

We can fix the droplet's eccentricity and viscosity ratio to observe that higher squirming propulsion (compared with an unbounded spheroidal squirmer) is achieved when $b \geq 1.5$ and $e_s = 0.3$, versus $e_s = 0.9$. However, in this range of b the speed is lower compared with an unbounded spheroidal squirmer. This observation is also valid for $b < 1.5$ and $\lambda < 1.25$. When $b \lessapprox 1.5$, $e_d = 0.3$ and $\lambda = 10$, our results reveal the only set of parameters

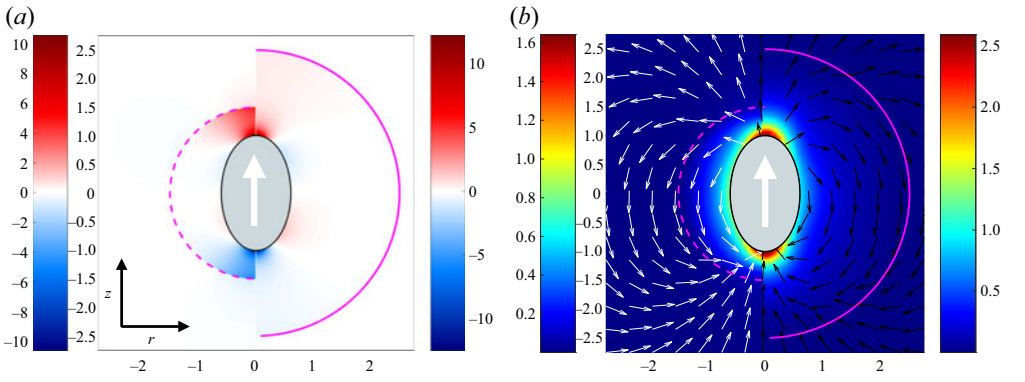

Figure 10. (*a*) Pressure and (*b*) flow field for the spheroidal squirmer in a spherical droplet in figure 7(*a*). The eccentricity $e_s = 0.8$ and the viscosity ratio $\lambda = 0.1$. In each panel, the left half represents $b = 1.5$ and the right half represents $b = 2.5$. The white arrow in the centre of the squirmer denotes the motion along the $\boldsymbol{e}_z$ direction.

for which the enclosed spheroidal squirmer propels faster compared with a spheroidal squirmer in an unbounded Newtonian domain (illustrated in figure 9*b*). More interestingly, the squirmer with high eccentricity ($e_s = 0.9$) now yields a larger speed compared with the squirmer with a low eccentricity ($e_s = 0.3$).

4.3. *Pressure and flow fields*

A close look at figure 7 reveals a number of interesting dynamics, such as (1) in figure 7(*a*) where larger (smaller) radial modes at $b = 1.5$ ($b = 2.5$) are observed for $e_s = 0.8$, (2) in figure 7(*f*) where smaller (larger) radial modes at $b = 1.5$ ($b = 2.5$) are observed for $e_d = 0.9$, and (3) the spherical squirmer in a spheroidal droplet with lower (higher) values of the radial modes at $b = 2.5$, $e_d = 0.9$ and $\lambda = 0.1$ ($\lambda = 10$) in figure 7(*d*) (figure 7*f*). In this section we investigate these features in more detail by contrasting the corresponding pressure and flow fields.

In figure 10 we show the pressure (figure 10*a*) and velocity field (figure 10*b*) for a spheroidal squirmer ($e_s = 0.8$) in a spherical droplet with viscosity ratio $\lambda = 0.1$. The left half of each panel represents the case with $b = 1.5$ while the right half shows the case with $b = 2.5$. We note that the propulsion speed (figure 8*a*) is higher at a lower droplet size. Moreover, the speed also increases with high eccentricity and $b = 1.5$ while remaining nearly independent of eccentricity for $b = 2.5$. The largest pressure and velocity magnitudes are concentrated at the front and back of the squirmer. The positive pressure distribution (yielding a compressive stress) at the front of the squirmer (which is weaker at $b = 1.5$ relative to $b = 2.5$) is consistent with the direction of swimming (indicated by the arrow). Moreover, the drag on the squirmer is larger at $b = 2.5$ (compared with $b = 1.5$), providing a plausible justification for the faster propulsion at low droplet size.

While the pressure distribution in the exterior of the droplet is zero for both S1 and S2, the distributions in the interior of the droplet are drastically different. Unlike S2, where the pressure is concentrated at the front and back of the squirmer and mostly sparse everywhere else, the pressure for S1 with $e_d = 0.9$ and $\lambda = 10$ (figure 11*a*) is distributed uniformly in the interior of the droplet, being zero only at the side of the squirmer. Figure 11(*b*) shows the flow field, where the left half of the panel represents the case with $b = 1.5$ and the right half shows the case with $b = 2.5$. As we observed previously,

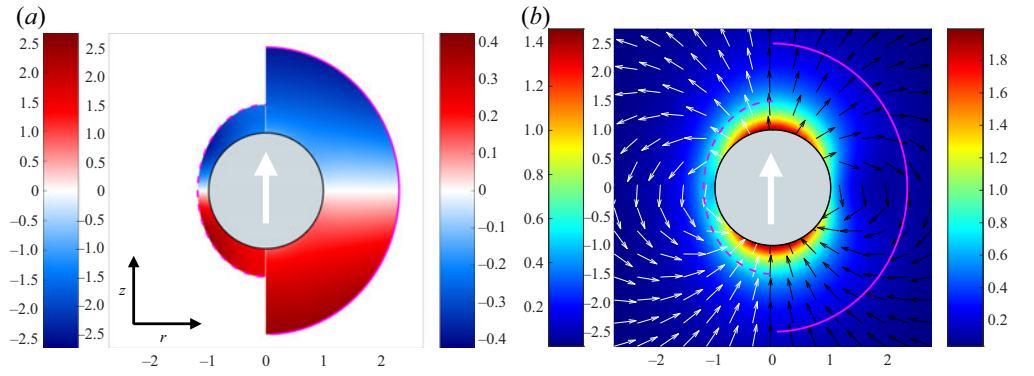

Figure 11. (*a*) Pressure and (*b*) flow field for the spherical squirmer in a spheroidal droplet in figure 7(*f*). The eccentricity $e_d = 0.9$ and the viscosity ratio $\lambda = 10$. In each panel, the left half represents $b = 1.5$ and the right half represents $b = 2.5$. The white arrow in the centre of the squirmer denotes the motion along the $\boldsymbol{e}_z$ direction.

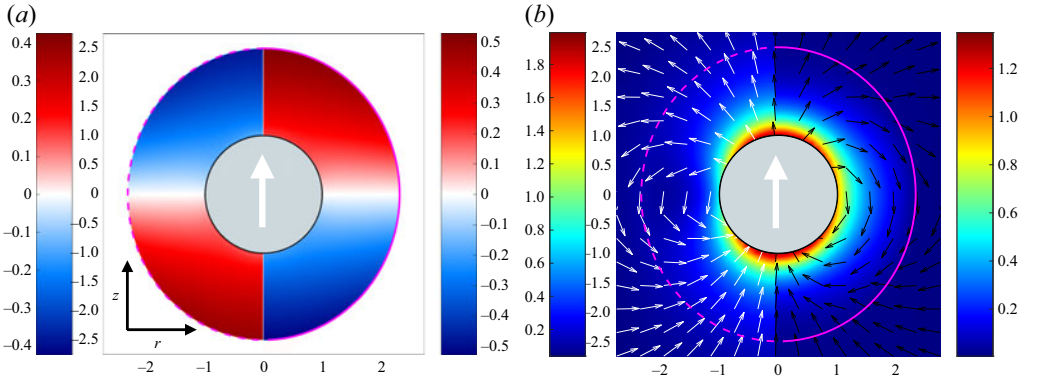

Figure 12. (*a*) Pressure and (*b*) flow field for the spherical squirmer in a spheroidal droplet in figure 7(*d*,*f*). The eccentricity $e_d = 0.9$ and the domain ratio $b = 2.5$. In each panel, the left half represents $\lambda = 10$ and the right half represents $\lambda = 0.1$. The white arrow in the centre of the squirmer denotes the motion along the $\boldsymbol{e}_z$ direction.

the front of the squirmer experiences the largest drag when $b = 2.5$ leading to a lower propulsion speed compared with $b = 1.5$.

Figure 12 shows the pressure (figure 12*a*) and flow (figure 12*b*) for S1 with $e_d = 0.9$ and $b = 2.5$. The left half of each panel has $\lambda = 10$ while the right half shows the case with $\lambda = 0.1$. The pressure field has the same order of magnitude for both values of the viscosity ratio. For $\lambda = 0.1$, positive pressure (corresponding to compressive stress) is observed at the front half of the squirmer, while negative pressure (corresponding to tensile stress) dominates at the rear half. The opposite holds for $\lambda = 10$: positive (negative) pressure at the back (front) of the squirmer. The positive pressure at the front of the squirmer for $\lambda = 0.1$ works against the forward motion of the swimmer. For this system, we found the propulsion speed to be one order of magnitude smaller at $\lambda = 0.1$ compared with $\lambda = 10$. A close inspection of figure 12(*b*) reveals a stronger flow field on the side of the squirmer (right half of the panel), indicating that the drag on the squirmer is higher at a low viscosity ratio (a plausible explanation for the lower propulsion speed).

5. Concluding remarks

We investigated the effects of heterogeneity or shape on the propulsion speed of a caged squirmer (a squirmer enclosed in a droplet). We particularly focused on neutral squirmers, since the propulsion speeds of an unbounded squirmer in a Newtonian fluid and heterogeneous medium considered here have been found to only depend on the first swimming mode B_1.

First, we considered a system consisting of a spherical squirmer enclosed in a spherical droplet that is immersed in a heterogeneous medium. We derived exact analytical solutions that recover the results of Reigh *et al.* (2017) in the limit of small fluid resistance ($\delta \to 0$). For a squirmer with a purely tangential mode and finite heterogeneity, our results show a non-trivial dependence of the propulsion speed on the droplet size, viscosity ratio and fluid resistance. We determined that the squirmer is always able to move inside the droplet for all values of the viscosity ratio and across the range of fluid resistance. These parameters combine in a non-trivial way to produce the observed squirmer's speed. In terms of co-swimming, both the mode ratio and speed depend on the structure of the medium being considered. The mode ratio shows two regions of near-constant values, being higher at lower fluid resistance. This indicates that, generally, the radial mode has less influence at large fluid resistance but is more prominent at low values of the fluid resistance.

Second, we numerically investigated the effects of various squirmer and droplet shapes on the propulsion in a Newtonian fluid. Specifically, we considered three distinct configurations: S1, a spherical squirmer in a spheroidal droplet; S2, a spheroidal squirmer in a spherical droplet; and S3, a spheroidal squirmer in a spheroidal droplet. These combinations revealed a rich number of dynamics, pointing to the critical influence of shapes. Compared with a squirmer in an unbounded Newtonian fluid, the propulsion speed shows a strong dependence on the viscosity ratio for a squirmer with purely tangential swimming modes in all three systems: it is lower for $\lambda = 0.1$ and higher for $\lambda = 10$. The systems are dissimilar in the way they respond to the squirmer's eccentricity: for S1, the drop's eccentricity only affects the spherical squirmer's propulsion at low b; for S2 and S3, the effects of the squirmer's eccentricity are reversed between low versus high viscosity ratios, although the drop's eccentricity in S3 does not yield any qualitative changes compared with S2. Regarding co-swimming in systems S1 and S2, we determined that the speed is always smaller compared with the squirmer in an unbounded Newtonian fluid. However, gain in speed closer to the optimal U_N can be achieved at high viscosity ratio and small droplet size. When factoring the dependence on eccentricity, shapes have the greatest effect for system S2 while S1 displays no significant changes as a result of varying the droplet's eccentricity. The squirmer is also always able to propel in S3. However, the size and eccentricity of the droplet greatly influences the propulsion speed, which nears zero for a large droplet size. We note, however, that in this system and for a smaller droplet size and eccentricity, the spheroidal squirmer is able to achieve propulsion speeds greater than that of its unbounded counterpart.

Our results provide important insights on the factors that affect the motion of microorganisms caged in a droplet. These insights in turn demonstrate how various designs could be employed to increase the effectiveness of carriers in drug delivery systems. In particular, knowledge of the environment's permeability can be incorporated to select the most optimal value of the radial mode that produces a co-swimming state. Alternatively, the size of the system could also be chosen strategically to achieve certain propulsion speeds. Exploring the stability of the squirmer/droplet systems is also of critical importance. Reigh *et al.* (2017) showed that the stability of the co-swimming state depends on the position of the squirmer relative to the droplet's centre, and on

the second swimming mode B_2. One would expect those results to hold in our study for low to moderate heterogeneity. However, the influence of high heterogeneity and/or shape on the stability remains to be investigated. Other natural extensions of our work involve combining both heterogeneity and shapes, including investigating the squirming of spheroidal shapes in an unbounded heterogeneous medium. These extensions will be explored in future studies.

Funding. U.A. and H.N. gratefully acknowledge funding support from the National Science Foundation, grant no. 2211633. H.N. also acknowledges support from a Jess and Mildred Fisher Endowed Professor of Mathematics from the Fisher College of Science and Mathematics at Towson University.

Declaration of interests. The authors report no conflict of interest.

Author ORCIDs.
E. Demir https://orcid.org/0000-0002-2099-1679;
H. Nganguia https://orcid.org/0000-0002-2107-2754.

Appendix A. Coefficients appearing in the flow field

The coefficients for the flow field obtained from (2.16) are

$$O = \frac{-2(b^2+b-2)(b\delta+3)-12\lambda}{(b-1)^2\mathcal{D}} + \frac{(b^3+3b-4)(b\delta+3)-6(b-2)\lambda}{(b-1)^3\mathcal{D}}\alpha + \frac{3b[(b^2-1)(b\delta+3)+2\lambda]}{(b-1)^3\mathcal{D}}U_S - \frac{6b[(b^4-b^3)\delta+b^3+\lambda-1]}{(b-1)^3\mathcal{D}}U_D, \tag{A1}$$

$$Q = \frac{2[6(b^5-1)\lambda+(3b^5-4b^4+3b^3-4b^2+2)(b\delta+3)]}{(b-1)^3\mathcal{D}} - \frac{6(b^5+4)\lambda+(3b^5+5b^3-8)(b\delta+3)}{(b-1)^3\mathcal{D}}\alpha - \frac{6(3b^5+2)\lambda+(9b^5-5b^3-4)(b\delta+3)}{(b-1)^3\mathcal{D}}U_S + \frac{2[5b^7\delta+b^6(6\lambda+9)-5b^4\delta+9b(\lambda-1)]}{(b-1)^3\mathcal{D}}U_D, \tag{A2}$$

$$R = -\frac{2b[6b^5\lambda+(2b^5-5b^2)(b\delta+3)+3b\delta-6\lambda+9]}{(b-1)^3\mathcal{D}} + \frac{2b[3(b^5+4)\lambda+(b^5+5b^2-6)(b\delta+3)]}{(b-1)^3\mathcal{D}}\alpha + \frac{6b[(b^5-1)(b\delta+3)+(3b^5+2)\lambda]}{(b-1)^3\mathcal{D}}U_S - \frac{3b[5b^6\delta+6b^5\lambda+9b^5-5b^4\delta-5b^3+4(\lambda-1)]}{(b-1)^3\mathcal{D}}U_D, \tag{A3}$$

$$
\begin{aligned}
S = {} & \frac{12b^5\lambda + (4b^5 - 2b^4 - 2b^3)(b\delta + 3)}{(b-1)^2\mathcal{D}} \\
& + \frac{6(b-2)b^5\lambda + 2(b^6 - 3b^5 + 2b^3)(b\delta + 3)}{(b-1)^3\mathcal{D}}\alpha \\
& - \frac{2[(b^6 - b^3)(b\delta + 3) + 3b^6\lambda]}{(b-1)^3\mathcal{D}}U_S \\
& + \frac{5b^7\delta + 6b^6\lambda + 9b^6 - 9b^5\delta + 4b^4\delta - 9b^4}{(b-1)^3\mathcal{D}}U_D,
\end{aligned} \tag{A4}
$$

$$
\begin{aligned}
T = {} & \frac{6b(b^2 + 3b + 1)(b\delta + 1)\lambda}{\delta^2\mathcal{D}} \\
& - \frac{3(b^4 + 2b^3 + 8b^2 + 4b)(b\delta + 1)\lambda}{\delta^2(b-1)\mathcal{D}}\alpha \\
& - \frac{3(3b^4 + 6b^3 + 4b^2 + 2b)(b\delta + 1)\lambda}{\delta^2(b-1)\mathcal{D}}U_S \\
& + \left\{ \frac{\begin{array}{l} 6\lambda[6b^5 + 6b^4 + b^3\delta + 6b^3 + 6(b^6 + b^5 + b^4)\delta \\ \quad + (2b^7 + b^6 - b^4 - 2b^3)\delta^2 - 4b^2\delta + b^2 - 4b] \end{array}}{2\delta^2(b-1)\mathcal{D}} \right. \\
& \left. + \frac{6\lambda(4b^3 + 7b^2 + 4b)(b-1)^2(b^4\delta^3 + 3b^3\delta^2 + 6b^2\delta + 6b)}{2\delta^2(b-1)\mathcal{D}} \right\} U_D,
\end{aligned} \tag{A5}
$$

$$
\begin{aligned}
W = {} & 3\sqrt{\frac{2}{\pi}}\mathrm{e}^{b\delta}\sqrt{b\delta}\left\{ -\frac{2(b^{5/2} + 3b^{3/2} + b^{1/2})\delta\lambda}{\mathcal{D}} \right. \\
& + \frac{(b^{7/2} + 2b^{5/2} + 8b^{3/2} + 4b^{1/2})\delta\lambda}{(b-1)\,\mathcal{D}}\alpha \\
& + \frac{(3b^{7/2} + 6b^{5/2} + 4b^{3/2} + 2b^{1/2})\delta\lambda}{(b-1)\,\mathcal{D}}U_S \\
& \left. - \frac{\sqrt{b}\delta[(6b^4 + 6b^3 + 6b^2 + b - 4)\lambda + (4b^2 + 7b + 4)(b-1)^2]}{(b-1)\mathcal{D}}U_D \right\},
\end{aligned} \tag{A6}
$$

where

$$
\mathcal{D} = 6(b+1)(2b^2 + b + 2)\lambda + (b-1)(4b^2 + 7b + 4)(b\delta + 3). \tag{A7}
$$

Appendix B. Droplet propulsion speed

Studies on the propulsion of a spherical squirmer with tangential surface velocity and enclosed in a clean (Reigh *et al.* 2017; Shaik *et al.* 2018) or surfactant-covered (Reigh *et al.* 2017; Shaik *et al.* 2018) droplet in a Newtonian fluid have shown that the squirmer always propels faster than the droplet. In investigating the effects of the medium's heterogeneity

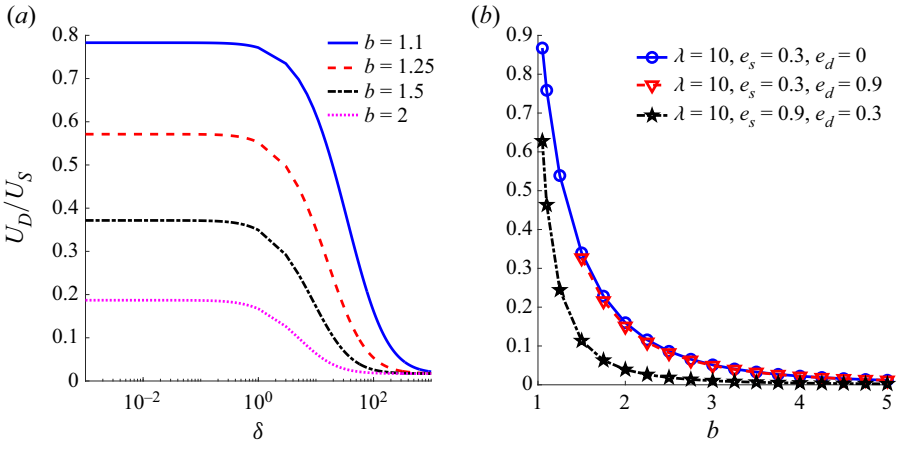

Figure 13. Ratio of droplet to squirmer propulsion speeds as a function of (*a*) the fluid resistance δ and (*b*) the droplet size b. In (*a*) the squirmer and droplet are spherical ($e_s = e_d = 0$) and the curves denote various values of the droplet size b. In (*b*) the fluid resistance $\delta = 10^{-3}$ and the curves denote various shape configurations. In both panels, the viscosity ratio $\lambda = 10$.

or both the squirmer and droplet's shapes, our results reveal that neither of these two factors yield droplet speeds larger than the squirmer's. These findings are consistent with the trend observed from those studies in the absence of heterogeneity and for a spherical squirmer and droplet. The figures for the droplet speed, scaled by the squirmer's speed, U_D/U_S are plotted as a function of the fluid resistance δ (figure 13*a*) and as a function of the droplet's size b (figure 13*b*). They show that the ordinate U_D/U_S is consistently less than 1 and monotonically decreasing to zero. The results imply that the squirmer speed is always larger independently of the fluid resistance or shape configurations. In the case of the dependence on δ, the droplet becomes motionless as $\delta \to \infty$, while the squirmer continues propelling (§ 3.2).

References

Blake, J.R. 1971 A spherical envelope approach to ciliary propulsion. *J. Fluid Mech.* **46**, 199–208.

Brinkman, H.C. 1949 Calculation of the viscous force exerted by a flowing fluid on a dense swarm of particles. *Appl. Sci. Res.* **1**, 27–34.

Celli, J.P., *et al*. 2009 Helicobacter pylori moves through mucus by reducing mucin viscoelasticity. *Proc. Natl Acad. Sci. USA* **106**, 14321–14326.

Chang, D., Ma, Y., Xu, X., Xie, J. & Ju, S. 2021 Stimuli-responsive polymeric nanoplatforms for cancer therapy. *Front. Bioengng Biotechnol.* **9**, 707319.

Chisholm, N.G., Legendre, D., Lauga, E. & Khair, A.S. 2016 A squirmer across Reynolds numbers. *J. Fluid Mech.* **796**, 233–256.

Clausal-Tormos, J., *et al*. 2008 Droplet-based microfluidic platforms for the encapsulation and screening of mammalian cells and multicellular organisms. *Chem. Biol.* **15**, 427–437.

Cooley, M., Strode, A., Hoore, M., Fedosov, D.A., Mitragotri, S. & Gupta, A.S. 2018 Influence of particle size and shape on their margination and wall-adhesion: implications in drug delivery vehicle design across nano-to-micro scale. *Nanoscale* **10**, 15350–15364.

Daddi-Moussa-Ider, A., Lowen, H. & Gekle, S. 2018 Creeping motion of a solid particle inside a spherical elastic cavity. *Eur. Phys. J.* E **41**, 104.

Datt, C., Zhu, L., Elfring, G.J. & Pak, O.S. 2015 Squirming through shear-thinning fluids. *J. Fluid Mech.* **784**, R1.

Ding, Y., Qiu, F., Solvas, X.C., Chiu, F.W.Y., Nelson, B.J. & DeMello, A. 2016 Microfluidic-based droplet and cell manipulations using artificial bacterial flagella. *Micromachines* **7**, 25.

FABOZZI, A., DELLA SALA, F., DI GENNARO, M., BARRETTA, M., LONGOBARDO, G., SOLIMANDO, N., PAGLIUCA, M. & BORZACCHIELLO, A. 2023 Design of functional nanoparticles by microfluidic platforms as advanced drug delivery systems for cancer therapy. *Lab on a Chip* **23**, 1389–1409.

GLUSHKOVA, D., CHOLAKOVA, D., BISEROVA, A., TSVETKOVA, K., TCHOLAKOVA, S. & DENKOV, N. 2023 Drop shape stability vs shape shifting: role of surfactant adsorption layer. *Colloid Surf.* A **656**, 130374.

VAN GOGH, B., DEMIR, E., PALANIAPPAN, D. & PAK, O.S. 2022 The effect of particle geometry on squirming through a shear-thinning fluid. *J. Fluid Mech.* **938**, A3.

GÓMEZ, S., GODÍNEZ, F.A., LAUGA, E. & ZENIT, R. 2017 Helical propulsion in shear-thinning fluids. *J. Fluid Mech.* **812**, R3.

GUO, H., ZHU, H., LIU, R., BONNET, M. & VEERAPANENI, S. 2021 Optimal slip velocities of micro-swimmers with arbitrary axisymmetric shapes. *J. Fluid Mech.* **910**, A26.

HAPPEL, J. & BRENNER, H. 1973 *Low Reynolds Number Hydrodynamics: With Special Applications to Particulate Media*. Noordhoff International.

HOELL, C., LOWEN, H., MENZEL, A.M. & DADDI-MOUSSA-IDER, A. 2019 Creeping motion of a solid particle inside a spherical elastic cavity: II. Asymmetric motion. *Eur. Phys. J.* E **42**, 89.

ISHIMOTO, K. & GAFFNEY, E.A. 2014 Swimming efficiency of spherical squirmers: beyond the Lighthill theory. *Phys. Rev.* E **90**, 012704.

JUNG, S. 2010 Caenorhabditis elegans swimming in a saturated particulate system. *Phys. Fluids* **22**, 031903.

KELLER, S.R. & WU, T.Y. 1977 A porous prolate-spheroidal model for ciliated micro-organisms. *J. Fluid Mech.* **80**, 259–278.

KEMP, J.A. & KWON, Y.J. 2021 Cancer nanotechnology: current status and perspectives. *Nano Converg.* **8**, 34.

KOLOSNJAJ-TABI, J., GIBOT, L., FOURQUAUX, I., GOLZIO, M. & ROLS, M.-P. 2019 Electric field-responsive nanoparticles and electric fields: physical, chemical, biological mechanisms and therapeutic prospects. *Adv. Drug Deliv. Rev.* **138**, 56–67.

KREE, R., RUCKERT, L. & ZIPPELIUS, A. 2021 Dynamics of a droplet driven by an internal active device. *Phys. Rev. Fluids* **6**, 034201.

KREE, R. & ZIPPELIUS, A. 2021 Controlled locomotion of a droplet propelled by an encapsulated squirmer. *Eur. Phys. J.* E **44**, 6.

LAUGA, E. 2007 Propulsion in a viscoelastic fluid. *Phys. Fluids* **19** (8), 083104.

LAUGA, E. 2016 Bacterial hydrodynamics. *Annu. Rev. Fluid Mech.* **48**, 105–130.

LEE, J.H. & YEO, Y. 2015 Controlled drug release from pharmaceutical nanocarriers. *Chem. Engng Sci.* **125**, 75–84.

LEIDERMAN, K. & OLSON, S.D. 2016 Swimming in a two-dimensional Brinkman fluid: computational modeling and regularized solutions. *Phys. Fluids* **28**, 021902.

LESHANSKY, A.M. 2009 Enhanced low-Reynolds number propulsion in heterogeneous viscous environments. *Phys. Rev.* E **80**, 051911.

LIGHTHILL, M.J. 1952 On the squirming motion of nearly spherical deformable bodies through liquids at very small Reynolds numbers. *Commun. Pure Appl. Maths* **5**, 109–118.

LISICKI, M., RODRIGUES, M.F.V., GOLDSTEIN, R.E. & LAUGA, E. 2019 Swimming eukaryotic microorganisms exhibit a universal speed distribution. *eLife* **8**, e44907.

LIU, Y., TAN, J., THOMAS, A., OU-YANG, D. & MUZYKANTOV, V.R. 2012 The shape of things to come: importance of design in nanotechnology for drug delivery. *Ther. Deliv.* **3**, 181–194.

MARSHALL, K.J. & BRADY, J.F. 2021 The hydrodynamics of an active squirming particle inside of a porous container. *J. Fluid Mech.* **919**, 259–278.

MIRBAGHERI, S.A. & FU, H.C. 2016 Helicobacter pylori couples motility and diffusion to actively create a heterogeneous complex medium in gastric mucus. *Phys. Rev. Lett.* **116**, 198101.

MITCHELL, M.J., BILLINGSLEY, M.M., HALEY, R.M., WECHSLER, M.E., PEPPAS, N.A. & LANGER, R. 2021 Engineering precision nanoparticles for drug delivery. *Nat. Rev. Drug Discov.* **20**, 101–124.

NEJATI, S., VADEGHANI, E.M., KHORSHIDI, S. & KARKHANEH, A. 2020 Role of particle shape on efficient and organ-based drug delivery. *Eur. Polym. J.* **122**, 109353.

NGANGUIA, H., DAS, D., PAK, O.S. & YOUNG, Y.N. 2023 Influence of surface viscosities on the electrodeformation of a prolate viscous drop. *Soft Matt.* **19**, 776–789.

NGANGUIA, H. & PAK, O.S. 2018 Squirming motion in a Brinkman medium. *J. Fluid Mech.* **855**, 554–573.

NGANGUIA, H., ZHENG, K., CHEN, Y., PAK, O.S. & ZHU, L. 2020*a* A note on a swirling squirmer in a shear-thinning fluid. *Phys. Fluids* **32**, 111906.

NGANGUIA, H., ZHU, L., PALANIAPPAN, D. & PAK, O.S. 2020*b* Squirming in a viscous fluid enclosed by a Brinkman medium. *Phys. Rev.* E **101**, 063105.

PAK, O.S., ZHU, L., BRANDT, L. & LAUGA, E. 2012 Micropropulsion and microrheology in complex fluids via symmetry breaking. *Phys. Fluids* **24**, 103102.
PALANIAPPAN, D. 2014 On some general solutions of transient Stokes and Brinkman equations. *J. Theor. Appl. Mech.* **52**, 405–415.
PEDLEY, T.J. 2016 Spherical squirmers: models for swimming micro-organisms. *IMA J. Appl. Maths* **81**, 488–521.
POHNL, R., POPESCU, M.N. & USPAL, W.E. 2020 Axisymmetric spheroidal squirmers and self-diffusiophoretic particles. *J. Phys.: Condens. Matter* **32**, 164001.
RADOLF, J. & LUKEHART, S. 2006 *Pathogenic Treponema: Molecular and Cellular Biology*. Caister Academic Press.
RAVESHI, M.R., HALIM, M.S.A., AGNIHOTRI, S.N., O'BRYAN, M.K., NEILD, A. & NOSRATI, R. 2021 Curvature in the reproductive tract alters sperm–surface interactions. *Nat. Commun.* **12**, 3446.
REIGH, S.Y. & LAUGA, E. 2017 Two-fluid model for locomotion under self-confinement. *Phys. Rev. Fluids* **2**, 093101.
REIGH, S.Y., ZHU, L., GALLAIRE, F. & LAUGA, E. 2017 Swimming with a cage: low-Reynolds-number locomotion inside a droplet. *Soft Matt.* **13**, 3161.
RODRIGUES, M.F.V., LISICKI, M. & LAUGA, E. 2021 The bank of swimming organisms at the micron scale (BOSO-Micro). *PLoS ONE* **16**, e0252291.
RUTLLANT, J., LOPEZ-BEJAR, M. & LOPEZ-GATIUS, F. 2005 Ultrastructural and rheological properties of bovine vaginal fluid and its relation to sperm motility fertilization: a review. *Reprod. Domest. Anim.* **40**, 79–86.
SAMANTA, D., HOSSEINI-NASSAB, N. & ZARE, R.N. 2016 Electroresponsive nanoparticles for drug delivery on demand. *Nanoscale* **8**, 9310.
SHAIK, V.A., VASANI, V. & ARDEKANI, A.M. 2018 Locomotion inside a surfactant-laden drop at low surface Péclet numbers. *J. Fluid Mech.* **851**, 187–230.
SPRENGER, A.R., SHAIK, V.A., ARDEKANI, A.M., LISICKI, M., MATHIJSSEN, A.J.T.M., Guzman-Lastra, F., Lowen, H., Menzel, A.M. & Daddi-Moussa-Ider, A. 2020 Towards an analytical description of active microswimmers in clean and in surfactant-covered drops. *Eur. Phys. J.* E **43**, 58.
TAYLOR, G.I. 1951 Analysis of the swimming of microscopic organisms. *Proc. R. Soc. Lond.* A **209**, 447–461.
THEERS, M., WESTPHAL, E., GOMPPER, G. & WINKLER, R.G. 2016 Modeling a spheroidal microswimmer and cooperative swimming in a narrow slit. *Soft Matt.* **12**, 7372.
WALL, M.A., HARMSEN, S., PAL, S., ZHANG, L., ARIANNA, G., LOMBARDI, J.R., DRAIN, C.M. & KIRCHER, M.F. 2017 Surfactant-free shape control of gold nanoparticles enabled by unified theoretical framework of nanocrystal synthesis. *Adv. Mater.* **29**, 1605622.
WEI, W., SUNG, J., GUO, X.-Y., CHEN, X., WANG, R., QIU, C., ZHANG, H.-T., PANG, W.-H., WANG, J.-C. & ZHANG, Q. 2020 Microfluidic-based holonomic constraints of siRNA in the kernel of lipid/polymer hybrid nanoassemblies for improving stable and safe in vivo delivery. *ACS Appl. Mater. Inter.* **12**, 14839–14854.
WEN, H., YU, Y., ZHU, G., JANG, L. & QIN, J. 2015 A droplet microchip with substance exchange capability for the developmental study of *C. elegans*. *Lab on a Chip* **15**, 1905–1911.
WOLGEMUTH, C.W. 2015 Flagellar motility of the pathogenic spirochetes. *Semin. Cell Dev. Biol.* **46**, 104–112.
WU, Z., CHEN, Y., MUKASA, D., PAK, O.S. & GAO, W. 2020 Medical micro/nanorobots in complex media. *Chem. Soc. Rev.* **49**, 8088–8112.
YU, T.S., LAUGA, E. & HOSOI, A.E. 2006 Experimental investigations of elastic tail propulsion at low Reynolds number. *Phys. Fluids* **18**, 091701.
ZHANG, J., LIU, H. & ZHANG, X. 2021 Modeling the deformation of a surfactant-covered droplet under the combined influence of electric field and shear flow. *Phys. Fluids* **33**, 042109.
ZHU, L., DO-QUANG, M., LAUGA, E. & BRANDT, L. 2011 Locomotion by tangential deformation in a polymeric fluid. *Phys. Rev.* E **83**, 011901.
ZLATANOVSKI, T. 1999 Axisymmetric creeping flow past a porous prolate spheroidal particle using the Brinkman model. *Q. J. Mech. Appl. Maths* **52**, 111–126.